

Nanogold plasmonic photocatalysis for organic synthesis and clean energy conversion

Cite this: *Chem. Soc. Rev.*, 2014, **43**, 7188

Changlong Wang and Didier Astruc*

Received 30th April 2014

DOI: 10.1039/c4cs00145a

www.rsc.org/csr

This review provides the basic concepts, an overall survey and the state-of-the art of plasmon-based nanogold photocatalysis using visible light including fundamental understanding and major applications to organic reactions and clean energy-conversion systems. First, the basic concepts of localized surface plasmon resonance (LSPR) are recalled, then the major preparation methods of AuNP-based plasmonic photocatalysts are reviewed. The major part of the review is dedicated to the latest progress in the application of nanogold plasmonic photocatalysis to organic transformations and energy conversions, and the proposed mechanisms are discussed. In conclusion, new challenges and perspectives are proposed and analyzed.

Introduction

Sunlight is a reagent of choice for “green” chemical synthesis due to its abundance, absence of cost, and environmentally friendly nature. Considerable efforts have been made to use sunlight as a driving force for chemical synthesis processes. However, the simple inability of most organic molecules to absorb light in the visible range of the spectrum has largely limited the potential applications of photochemical reactions.¹ Thus, the design of highly efficient photocatalysts should bring significant progress in fine chemical synthesis, as exemplified by the recent review on general organic photocatalysis by Zhao’s group.²

Gold nanoparticles (AuNPs) have been extensively studied because of their unique optical and electronic properties together with their various applications in electronics, photonics, catalysis, and nano- and biotechnology.^{3–5} Triggered by their unprecedented catalytic properties, AuNPs have also attracted tremendous interest in the past years in both heterogeneous^{6–8} and homogeneous catalysis.⁹ Recently, the localized surface plasmon resonance (LSPR) effect of nanostructured materials,¹⁰ for example noble Au and Ag nanoparticles (NPs),¹¹ and Cu^{12–14} NPs, has been successfully applied to photocatalysis under visible light irradiation and proved to be promising. Therefore, in the present review, we are selectively dealing with plasmonic nanogold photocatalysis. We mainly focus on five aspects: (i) basic concepts of the LSPR effect of metal NPs, (ii) AuNP-based plasmonic photocatalyst preparation methods,

ISM, Univ. Bordeaux, 351 Cours de la Libération, 33405 Talence Cedex, France.
E-mail: d.astruc@ism.u-bordeaux1.fr



Changlong Wang

Changlong Wang was born in Shandong province, China. He carried out graduate studies in materials processing engineering with Prof. Dezhi Wang at Central South University in Changsha, China. Then, he joined the research group of Prof. Didier Astruc at the University of Bordeaux, France, in 2013. His research interests are in the areas of the functionalization and engineering of gold nanoparticles for applications in nanomaterials and catalysis.



Didier Astruc

Didier Astruc was born in Versailles and studied in Rennes where he passed his PhD with Prof. R. Dabard. He did a post-doc at MIT in Cambridge, Mass. with Prof. R. R. Schrock and a sabbatical leave in the University of California at Berkeley with Prof. K. P. C. Vollhardt. He is a full Professor at the University of Bordeaux and a Member of the Institut Universitaire de France and various Academies. His research interests are in inorganic chemistry and nano-materials including catalysis, sensors, molecular electronics and nanomedicine (<http://astruc.didier.free.fr/welcome.htm>).

(iii) recent developments in the efficient AuNP-based plasmonic photocatalysis for organic synthesis, (iv) application of plasmon photocatalysis to energy conversions processes that are driven by visible-light, and (v) possible mechanisms of LSPR-enhanced photocatalytic activity. Finally, the challenges and potential future applications will be highlighted.

1 Basic concepts of the LSPR effect of metal NPs

The century-old Mie's theory defines the LSPR as the resonant photon-induced coherent oscillation of charges at the metal-dielectric interface that is established when the photon frequency matches the natural frequency of the metal surface electrons oscillating against the restoring force of their positive nuclei.¹⁵ Simply, LSPR is made up of collective oscillations of free electrons in metal NPs driven by the electromagnetic field of incident light and because of which metallic NPs absorb visible and infrared light in particular regions.¹⁶ For example, Au, Ag and Cu NPs show a strong photoabsorption of visible light due to their surface plasmon that displays maxima at approx. 530, 400 and 580 nm, respectively. However, nanostructured copper and silver are easily oxidized, whereas AuNPs are more chemically stable and resistant in the presence of oxygen. The LSPR, a characteristic of NPs with conduction bands, is not observed for such clusters that are smaller than 2 nm, because the latter are molecules that are defined by localized molecular orbitals. It is around this 2 nm-size that one finds the progressive transition between the molecular state (cluster molecules with only a few tens of atoms) and the nanometallic state defined by conduction bands with a large (or very large) number of atoms in nanoparticles up to the order of 200 nm. Thus, this unique plasmonic absorption that characterizes larger noble metal NPs has been used for a variety of applications including sensors,¹⁷ solar cells,¹⁸ nanomedicine^{19–22} and theranostics (therapeutics + diagnostics), especially for cancer treatment.²³ Very recently, researchers have successfully introduced this unique property in the new field of plasmonic photocatalysts in order to catalyze organic reactions²⁴ and water splitting.²⁵ Plasmonic photocatalysis has offered a new opportunity to solve the problem of the limited efficiency of photocatalysts and photovoltaic devices. In these reactions, the nanostructured plasmonic metals are often combined with a semiconductor-based material (e.g., TiO₂ and ZrO₂, namely plasmonic photocatalysts), and the catalytic activity and efficiency are greatly enhanced due to the SPR effect that improves the solar-energy-conversion efficiency in three aspects:²⁶ (i) the near-field enhancement of localized plasmons, (ii) the increase of the scattering effect, and (iii) the excitation e^-h^+ pairs in the semiconductor due to the plasmonic energy transfer from the metal to the semiconductor.

1.1 Fundamentals of the LSPR

The basis of the LSPR effect has been described in a recent review by Mayer and Hafner,²⁷ and the detailed illustrations of the mechanisms of the plasmonic enhancement to photocatalysis

have been shown by Zhang *et al.*²⁸ These two reviews provide understanding of the physical principles of the LSPR, and hereafter we therefore only give a short introduction. When a small spherical metallic NP is illuminated by light (with a wavelength far exceeding the NP size), the electron decreases on the one side of the NP and increases on the other side. This causes the redistributions of the charge density, and the distributed charge density creates an electric field inside and outside the metal NP with a direction that is opposite to that of the electric field of the light. During the process of the displacement of electron density, the coulombic restoring force that is caused by the oscillations in the NP is established, and the resonance between the oscillations and the incident light is known as the LSPR (Fig. 1a).²⁹ Thus, LSPR endows the metal nanocrystals with very large absorption and scattering cross-sections and local electromagnetic field enhancement in the near-field region near the surface of plasmonic metal nanocrystals.

When the wavelength of the incident light is in the range of the LSPR absorption of noble metal NPs, the energy level reached by the electrons excited by LSPR is observed, and these electrons are excited to a higher state. For example, the resonance energy of AuNPs usually occurs in the visible range (e.g., 530 nm, however depending on the AuNP size, shape, and diffraction index of the medium). The interaction between the resonant photons and the surface electrons results in a high absorption coefficient of photons in resonance with plasmon excitation and capacitive coupling between clusters of plasmonic AuNPs.^{30,31} Thus, upon irradiation with visible light, through the excitation of LSPR of AuNPs, the energetic electrons are redistributed to the energy levels above the Fermi level. A strong electric field and a high concentration of energetic electrons are then formed or produced at the AuNP surface. These light excited energetic electrons remain in the excited "hot" state for up to 0.5–1 ps,^{32,33} they gain enough energy under visible light irradiation to activate reactant molecules adsorbed on the AuNPs and induce chemical reactions. Plasmon-excited NPs were proved to be an efficient

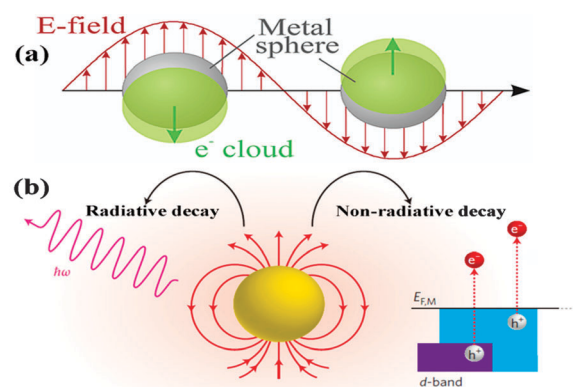


Fig. 1 (a) Schematic of SPR in a small spherical metallic NP that is irradiated by light, reprinted with permission from ref. 29. Copyright 2003 American Chemical Society. (b) Surface-plasmon decay processes, localized surface plasmons can decay radiatively via re-emitted photons (left), or non-radiatively via excitation of hot electrons (right). Reprinted with permission from ref. 39. Copyright 2014, Nature Publishing Group.

source of hot electrons through plasmon decay, because the direct excitation of hot electrons usually requires large incident light intensities.^{34–38} Plasmon excitation decaying processes through different pathways deposit energy into adsorbates, and the energy transfer from the plasmonic metal NPs to the adjacent semiconductors plays a crucial role in the photocatalytic functions. Following the dynamics of the LSPR and depending on the NP size and radiance of the plasmon, the coherent oscillation of electrons (plasmon quantum) decays by two competitive pathways.^{28,30,35,39} One is the radiative plasmon decay process (Fig. 1b left) that is dominant for AuNPs that are larger than 40 nm⁴⁰ and results in scattering. After the radiative plasmon decay process, the plasmon quantum decays into a photon. However, the efficiency of emission of the photon during this process has proved to be very low. Previous studies showed that the luminescence quantum yields were only 10^{−6} and 10^{−4} for Au nanospheres⁴¹ and Au nanorods,⁴² respectively. Thus, this low yield excludes the radiative energy transfer from the major contributors of the plasmonic enhancement.²⁸ The other pathway is the non-radiative decay process (Fig. 1b right), which is dominant for small NPs and enhances absorption, resulting in the excitation of energetic electrons and holes in the metal NPs. For instance, Au nanocrystals in the size of 10–20 nm are efficient for the generation of hot electrons with overbarrier energies.⁴³ In noble-metal nanostructures (e.g., Au and Ag NPs), non-radiative decay occurs through intraband excitations within the conduction band or through interband excitations resulting from transitions between other bands (e.g., d bands) and the conduction band.³⁹

The generation and injection of hot electrons are of great importance in understanding the mechanism of plasmon-assisted chemistry. The plasmon-induced hot electron injection efficiency is enhanced by controlling the size and shape of the plasmonic nanostructure.⁴⁴ The generation and injection of hot electrons will be discussed in more detail. Following the absorption of a photon, a free electron of the metal NP is excited to a higher energy level. The single electronic excitation will occur from below the metal Fermi level (E_F), creating a constant probability distribution of finding primary excited electrons at the energy level between the E_F and $E_F + h\nu$.³⁰ The electron may then quickly lose energy through the electron–electron scattering within ~ 10 fs after the initial plasmon excitation,⁴⁵ leading to a cascading process redistributing the energy of the primary electron to the electronic gas and creating a non-equilibrium Fermi–Dirac electron distribution. In this excitation and energy redistribution process, hot electron transfer may have two different pathways:⁴⁶ (1) hot electrons transfer from the metal NP tunnels into the lowest unoccupied molecular orbital (LUMO) of the adsorbed molecule located nearby the metal NP, or (2) hot electrons transfer from the metal NP to the contacted semiconductor. In this case, the equilibration of the E_F causes bending of the semiconductor conduction band and formation of a Schottky barrier that blocks electron transfer from the metal to the semiconductor. By the LSPR decay processes, hot electrons with energies higher than the Schottky barrier energy are injected into the adjacent semiconductor with an emission efficiency that depends on their energy.⁴⁷

After this process, due to electron depletion, the plasmonic nanostructures are left positively charged. To keep the charge balance and sustain an electric current, the carrier generation takes place in the presence of the electron-donor solution or a hole-transporting material, which should be in contact with the nanostructures to transport the generated holes to the counter electrode. Otherwise, the injected hot electrons decay back to the NP.³⁹ Hot electrons may then undergo a relaxation step through electron–phonon coupling⁴⁸ or scatter into an excited state of the molecular adsorbates. Thus, the activation energy of a specific photochemical reaction is reduced. As demonstrated by Nordlander's group, the activation energy of the photocatalytic dissociation of H₂ over Au/TiO₂ is reduced from 4.5 eV to 1.7–1.8 eV.³⁵ However, a question raised here is whether the reaction occurs on the AuNP surface or on the TiO₂ surface. In order to answer this question, recent work from this research group showed that, by changing the support from TiO₂ to SiO₂, due to the Schottky barrier at the Au/TiO₂ surface facilitating the hot-electron transfer into the TiO₂ matrix, the number of electrons available for the H₂ dissociation is reduced. Consequently, an almost two orders of magnitude H₂ dissociation rate improvement was observed on Au/SiO₂ samples compared to Au/TiO₂.⁴⁹ Thus, it appears that dissociation takes place on the illuminated AuNP surface, because plasmon decay transfer to the H₂ molecules substantially reduces the barrier for H₂ dissociation. In parallel with the cascading processes of electron energy spreading, photoexcited electrons with low energy relaxation through electron–photon collision lead to an increase of temperature of metal NPs, heating the local surrounding environment and/or the semiconductor and transferring energy to adsorbates.^{28,30}

Plasmonic nanostructures showed promise in manipulating light absorption in photocatalytic systems. For example, Fe₂O₃ is a kind of photocatalyst with a low band gap of 2.2 eV, making the usage of visible light difficult. However, as reported by Yang's group,⁵⁰ by taking the advantage of both the LSPR effect of Au nanopillars in the visible range and low band gap of the active semiconductor Fe₂O₃, a net photocurrent enhancement of about 50% for photoelectrochemical water splitting over the solar spectrum was obtained. This showed a promising way to produce renewable hydrogen fuel from solar energy by introducing the plasmonic nanostructures. The LSPR also enhances local electric field and the electron–hole pair generation. However, the detailed charge carrier transfer process is not fully understood. For example, in the decomposition of organic compounds under visible light, the observed enhancement of the reaction rate was attributed to direct charge carrier transfer,^{51–53} the local heating effect^{54–56} and radiative photon transfer.^{11,57} Thus, the interaction between the electronic charge carrier and the adsorbate plays a crucial role in the photocatalytic functions. It is widely accepted that in the charge transfer mechanism charge carriers are directly injected from excited plasmonic metal NPs into the adjacent semiconductor surface.²⁸ This ultrafast charge carrier transfer is ascribed to the direct contact between plasmonic NPs and the semiconductor. Due to the similarity between this charge transfer mechanism and the sensitization of semiconductors by organic dyes,^{58,59} this mechanism is also

called the “LSPR sensitization effect”. In addition to the local electric field enhancement mechanism, one part of emitted light is scattered to the far field while the other is concentrated at the metal surface. The LSPR mediates an indirect charge carrier transfer between plasmonic metal NPs and the semiconductor. The intensity of the local electromagnetic field is several orders of magnitude larger than that of the far-field incident light, and the highest charge carrier formation is observed at the semiconductor/liquid interface, which benefits the photocatalytic reactions.⁶⁰ The local electric field enhancement caused by the plasmon excitation is strongly dependent on the shape of the metal nanocrystal. Also, the distance between the plasmonic metal NPs affects the enhancement of the near field, because the increasing distance between the metal NPs leads to a decrease of the influence of the hot spot.⁶¹ Furthermore, plasmon coupling forms a “hot spot” region where more charge carriers are formed and easily couple with chemisorbed molecules of the photocatalytic system, leading to an efficient charge transfer. Thus, the magnitude of the near field intensity is several orders larger than that at the interface of the metal NP and the semiconductor. To make it clear, the detailed illustrations of these mechanisms and their related examples are discussed in Section 4. In addition, the LSPR is responsible for the electromagnetic (EM) field enhancement that also leads to surface-enhanced Raman scattering (SERS), which is related to rough surfaces or small metallic particles,⁶² and other surface-enhanced spectroscopic processes. This enhancement is very effective, and theoretical simulations have predicted that the intense EM field produced near the plasmon resonant metallic NPs leads to 10^{10} SERS enhancement,^{63,64} and even $>10^{13}$ for special silver nanoparticle array structures

at specific locations in the structure.⁶⁵ The methods and models were used to study the EM of Au and Ag NPs, with an emphasis on the determination of the extinction and SERS spectra that were reviewed by Schatz's group.⁶⁶ In the EM SERS excitation mechanism, due to its requirement of bond polarizability, however a chemical reaction is less likely to be induced compared to adsorbate photon absorption *via* allowed electronic transitions.³⁰

1.2 Influencing factors

In general, the LSPR usually occurs in small NPs in which the resonant wavelength and LSPR intensity are influenced by many factors. We will pick up the factors that are most important to the final photocatalytic performance such as the NP size, the shape of the NP and the surrounding environment (including the solvents). By precise control of the size, shape, and environment of a plasmonic metal nanostructure, it is possible to design efficient plasmonic photocatalysts for applications that were previously considered impossible.⁶⁰

1.2.1 AuNP size. For a plasmonic metal NP of a given shape, the LSPR features strongly depend on the NP size. By tailoring the size of the NP, the ratio of absorption to scattering, the number of LSPR modes and the LSPR peak position are greatly changed to obtain a desired LSPR effect, which results in improved catalytic functions.^{67–69} Therefore, when applying the LSPR effect to chemical reactions, the size effect on the LSPR properties must be carefully considered.

AuNPs with a diameter in the range of 10 nm have a strong LSPR absorption maximum at around 520 nm (Fig. 2a).⁷⁰ However, when the AuNPs reach 10–40 nm, they show a sharp absorption band in the 520–530 nm region, and further increase in the size in the range of 40–80 nm leads to a LSPR wavelength

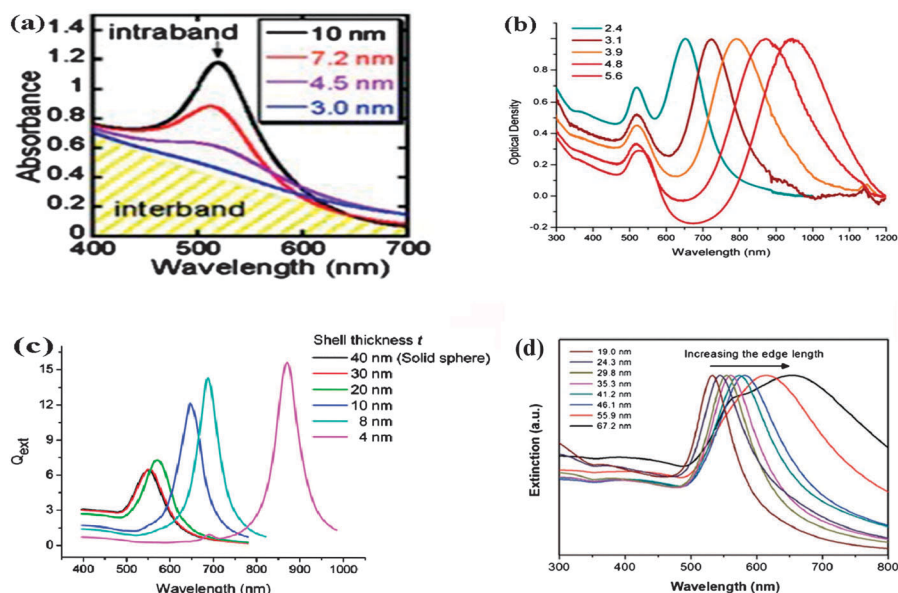


Fig. 2 Size-dependent effect on the LSPR absorption of AuNPs with different shapes. (a) Gold nanospheres. (b) AuNRs with various aspect ratios. (c) Plasmon resonance frequency calculated using Mie theory of silica core-AuNSs upon changing the shell thickness. Reprinted with permission from ref. 70, 74 and 76, respectively. Copyright 2006–2007, American Chemical Society (d) UV-vis extinction spectra of Au rhombic dodecahedra with different edge lengths. Reprinted with permission from ref. 78. Copyright 2013, Royal Society of Chemistry.

of 530–540 nm.⁷¹ Moreover, as the size of gold nanosphere increases, there is a red-shift in the LSPR due to a low frequency for the collective oscillation of electrons, which causes electromagnetic retardation in larger particles.^{67,72}

The association of AuNP size and LSPR properties has also been examined for other nanostructures of gold that are anisotropic,⁷³ such as Au nanorods, Au nanoshells and Au rhombic dodecahedra. In the case of gold nanorods (AuNRs), the SPR absorption maximum is shifted by either the change in size or aspect ratio, which is due to rod-shaped AuNPs usually having two kinds of resonance: one in the transverse direction and the other in the longitudinal direction, which is more sensitive to the aspect ratio. As shown in Fig. 2b, when the aspect ratio of gold nanorod increases, the SPR absorption band along the longitudinal direction shifts from the visible to the near infrared (NIR) region. Gold nanorods with an aspect of 3.9 show absorption overlapping with a region of minimum extinction of the human tissues,⁷⁴ and the AuNR aspect ratio can be tailored by using various methods.⁷⁵

Gold nanoshells (AuNSs) are a new kind of nanoparticles that often comprise a dielectric core such as silica, coated with an ultrathin gold layer. Therefore, the LSPR response of AuNSs is often associated with the relative size of the core and the thickness of a gold shell. Fig. 2c shows the plasmon resonance frequency of 80 nm silica core-AuNSs upon changing the shell thickness relative to the core size. Starting from a 40 nm solid AuNS, when decreasing the gold shell thickness, the LSPR red-shifts from the visible to the NIR region, and the plasmon band extinction increases. In addition, when the gold shell thickness is 4 nm, a small shoulder at around 690 nm is noticeable, corresponding to the quadrupolar/higher-order resonance mode.⁷⁶ Furthermore, the thickness of the Au nanoshell layer, core size and the surrounding medium all played determining roles in the absorption and scattering efficiencies of the LSPR wavelength of semiconductor-coated Au nanoshells.⁷⁷

The size and shape uniformity of the Au rhombic dodecahedra results in LSPR peaks of Au rhombic dodecahedra with relatively small sizes in the very narrow and sharp range.⁷⁸ As shown in Fig. 2d, when the edge length of the Au rhombic dodecahedra gradually increased from 19.0 to 24.3, 29.8, 35.3, 41.2 and 46.1 nm, their LSPR peaks were red shifted from 532 to 544, 554, 561, 574 and 582 nm, respectively. Moreover, as the edge length of Au rhombic dodecahedra further increases (from 55.9 to 67.2 nm), the LSPR peak substantially broadens, and a shoulder becomes noticeable. These features are attributed to the interactions between dipole resonances in larger Au nanocrystals and the wide size distributions in the larger size of Au rhombic dodecahedra. Furthermore, the trend of the LSPR peak position and the edge length of Au rhombic dodecahedra show linear relationships that are not well-fitted.

1.2.2 AuNP shape. Generally, the shape changes are also associated with the size changes in nonspherical nanostructures. Since the surface geometry varies with the shape, causing a shift in the electric field density on the surface, the resulting oscillation frequency of the electrons also changes, thereby generating different cross-sections of the LSPR properties.⁷⁹

In the case of the silver nanoparticles, Mock and his co-workers have investigated the shape effect of individual colloidal AgNPs on the LSPR properties.⁸⁰ By using high-resolution transmission electron micrographs (HRTEM) and optical spectroscopy, they compared the optical plasmon resonant properties of various AgNPs shapes and concluded that the geometrical shape played a major role in determining the plasmon resonance, while the increase in particles size was responsible for the spectrum red-shifts. Xia *et al.* have discussed the relationship between the plasmonic properties of Ag nanostructures and the size, shape, morphology and chemical composition, providing a better understanding of the effect of these parameters on the LSPR properties of AgNPs.⁶⁷ For AuNPs however, even in the same diameter of Au nanospheres and AuNSs, the refractive index sensitivities are different. AuNSs with a mean diameter of 50 nm exhibit almost 7 times larger red-shift for the SPR band compared to their sphere counterparts. In addition, this greatly improved sensitivity in optical response, making AuNSs very promising optical probes for chemical or biological binding events at solid-liquid interfaces.⁸¹

1.2.3 Surrounding environment. The LSPR absorption is also tuned by the surrounding dielectric environment that is influenced by the solvent effect and substrate effect.²⁹ For example, Ghosh *et al.*⁸² synthesized surfactant-stabilized AuNPs and measured the LSPR spectra of AuNPs that were exposed to various solvents. By comparison, they divided the solvent influences into two aspects: on the one hand, solvents (*e.g.*, cyclohexane, chloroform, carbon tetrachloride, toluene, and *o*-xylene) that do not possess any active functional group that change the refractive index at the NP/bulk interface; on the other hand, solvents such as acetonitrile (CH₃CN), tetrahydrofuran (THF), 1,4-dioxane, dimethylformamide (DMF), and dimethyl sulfoxide (DMSO) having nonbonding electrons that can coordinate to the AuNP surface, which influences the LSPR. Moreover, the shift in λ_{max} of the LSPR absorption depends on the AuNP core to ligand shell volume ratio, which is attributed to the change in the local dielectric environment upon introduction of the stabilizing ligands.

Apart from the influencing factors discussed above, other parameters such as the intensity and wavelength of the incident light^{83,84} also affect the LSPR properties. Furthermore, a discussion of the thermal effect is also necessary in order to evaluate the photocatalytic activity of Au based plasmonic photocatalysts (see Section 3.1.6). When introducing the LSPR effect into, for example, photocatalysts in a specific reaction, these factors should be comprehensively considered in order to obtain a better catalytic activity and modify product selectivity.

2 Methods of preparation of AuNP-based plasmonic photocatalysts

The components of the plasmonic photocatalysis are the plasmonic NPs, *e.g.* AuNPs and AgNPs, and the semiconductors. The photocatalytic reactions are initiated as a result of excitation of electrons in plasmonic metals by LSPR under visible light absorption,

during which LSPR boosts the generation of electrons and holes in semiconductor photocatalysts.²⁸ Also, the LSPR enhances the UV absorption of the large-bandgap materials.⁸⁵ Various methods and approaches are used to form this combined structure. Herein, we select the most frequently used methods of preparation of AuNP-based plasmonic photocatalysts, and related examples are discussed.

2.1 Deposition-precipitation (DP) method

Among various AuNP-based plasmonic photocatalyst preparation methods, the one that is the most frequently used is the deposition-precipitation method that is usually followed by further washing and reduction. In a typical synthetic procedure, the supporting material is immersed into the aqueous solution of HAuCl₄, followed by adding the solution (e.g. NaOH) to bring the resulting suspension to a required pH value by continuously stirring for a certain time. Then the precursor of the catalysts is recovered, filtered and washed with deionized water to hopefully completely remove the Cl[−] ions. Finally, the powder is calcinated at different temperatures under a certain atmosphere to obtain the catalyst. Size control of the Au-based plasmonic photocatalysts that are prepared by the DP method is very important: it is conducted by careful control of the loading amount of gold, and the calcination temperature can lead to very small size and narrow size distributions of the supporting materials. Tsukamoto *et al.*⁸⁶ have shown that when the Au loading is increased from 0.5 wt% to 2 wt%, 3 wt% and 5 wt%, the d_{Au} is gradually increased from 2.4 nm to 3.7, 4.9 and 7.8 nm, respectively, at the same calcination temperature. Generally, in the case of AuNPs loaded on TiO₂, a higher calcination temperature causes a larger AuNP size and sintering on the interphase between them. Interestingly, at a constant amount of Au loading, a higher calcination temperature not only leads to larger AuNPs but also changes their location. That is, at higher temperature (e.g., 673 K), AuNPs preferably locate at the anatase/rutile interface, and there is a well-defined contact surface for the Au/anatase/rutile phase (Fig. 3). Moreover, in the deposition step, the pH is also a key factor in determining the size distributions of the AuNPs. At the same calcination temperature, an increase of the pH value leads to a narrower size distribution.⁸⁷

2.2 Photoreduction (PR) method

Generally, when a semiconductor is irradiated with light of appropriate wavelength, the electrons in the valence band (VB) are photoexcited into the conduction band (CB), leaving positive holes in the VB. The electrons can then be used to reduce Au³⁺/AuCl₄[−] to Au⁰ that is deposited on the semiconductor, while the holes are captured by the scavenger to prevent accumulation of positive charges. Probably the most outstanding advantage of this method is that it provides a high deposition ratio of gold. The deposition ratio of Au species and both Au and Pd species can be larger than 99.9% for Au/CeO₂ catalysts²⁴ and Au@Pd/TiO₂ catalysts,⁸⁸ respectively, under irradiation with light of $\lambda > 300$ nm. However, the average AuNP size can be very large using the photoreduction method. Tanaka and his co-workers synthesized Au/CeO₂ catalysts by using two different kinds of

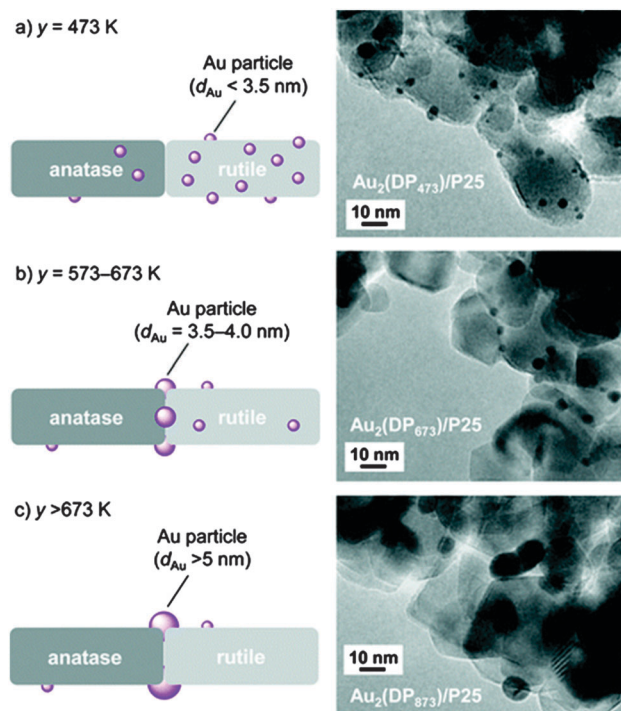


Fig. 3 Effect of the calcination temperature on the location and size of AuNPs on P25 TiO₂ and typical TEM images of Au₂(DP_y)/P25 catalysts prepared by the DP method, y stands for the calcination temperature. Reprinted with permission from ref. 86. Copyright 2012, American Chemical Society.

photoreduction methods, namely the single-step (SS) and multistep (MS) photodeposition methods. As shown in Fig. 4, the average particle sizes of SS- and MS-Au(1.0)/CeO₂ catalysts are 59.3 ± 4.9 and 92.1 ± 8.0 nm, respectively, indicating that the size of AuNPs-loaded CeO₂ on is strongly affected by the type of photoreduction method, and the MS photoreduction method tends to form larger AuNPs.²⁴ Their recent work shows that the MS photodeposition method leads to the co-existence of large (> 10 nm) and small (< 5 nm) AuNPs. Au size distribution and Au/TiO₂ photoabsorption are controlled by the times of photodeposition, post-calcination and TiO₂ properties.⁸⁹ Furthermore, in order to prepare a AuNP-based plasmonic photocatalyst, this method is often used alone or combined with other synthesis methods, for example with the DP method and is therefore called the deposition-precipitation-photoreduction method.⁵³

2.3 Encapsulation

The encapsulation of AuNP-based plasmonic photocatalysts usually corresponds to composite photocatalysts and core-shell nanostructure photocatalysts with the AuNPs as the core and the semiconductors as the shell. Encapsulation is not a typical method for the preparation of catalysts, but it is just a way to process or fabricate the catalyst composites that are often achieved by using other techniques. However, encapsulation is very useful, because it prevents the agglomeration and the growth of AuNPs and leads to the enhancement of long-term stable photocatalytic activity.²⁸ Recently, Zhang *et al.* designed and synthesized a sandwich-structured SiO₂/Au/TiO₂ plasmonic

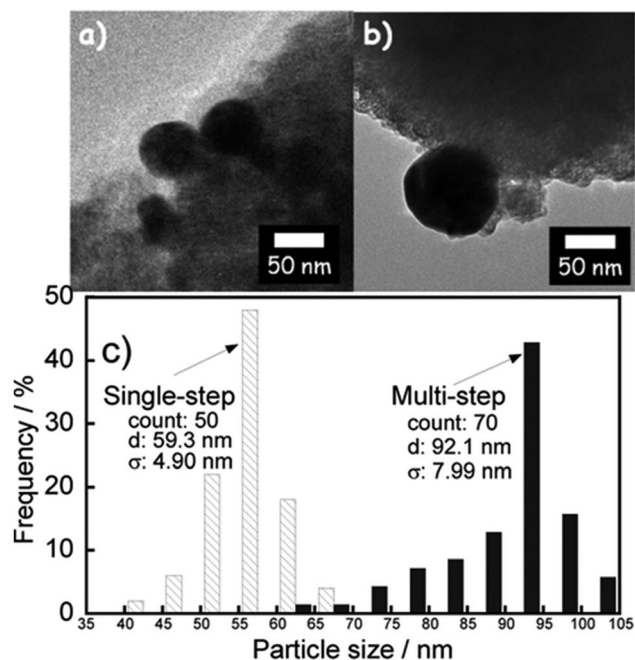


Fig. 4 Transmission electron micrographs (TEM) images of (a) SS-Au(1.0)/CeO₂, (b) MS-Au(1.0)/CeO₂, and (c) size distributions of Au particles of SS- and MS-Au/CeO₂ catalysts. Reprinted with permission from ref. 24. Copyright 2012, American Chemical Society.

photocatalyst that comprised a SiO₂ core, a AuNPs layer and a dropped TiO₂ nanocrystalline shell, by combining simple sol-gel and calcination processes. The fabrication of the SiO₂/Au/TiO₂ sandwich structures is depicted in Fig. 5. In the synthesis procedure, SiO₂ NPs with an average diameter of 400 nm are first synthesized, followed by incorporating the AuNPs with controlled loading and location in the sol-gel process, then introducing the TiO₂ matrix and calcinating to form the sandwich structure. This well-designed structure makes the SiO₂/Au/TiO₂ plasmonic photocatalyst very efficient in catalyzing the decomposition of organic compounds under UV, visible-light and natural-sunlight irradiation.⁹⁰

Very recently, another particular example of the core-shell and sandwich structures has been clearly demonstrated by Cushing *et al.*⁹¹ As shown in Fig. 6, first of all, Au nanospheres with an average diameter of 20 nm were synthesized (Fig. 6a). Then, Au@SiO₂ and Au@Cu₂O core-shell structures were successfully formed by coating AuNSs with ~5 nm thick SiO₂ layer and a ~25 nm thick Cu₂O layer, respectively (Fig. 6b and c).

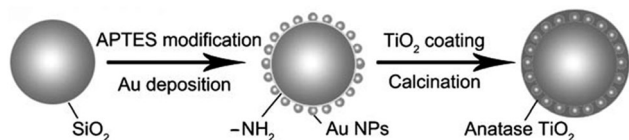


Fig. 5 Schematic illustration of the fabrication process of a sandwich-structured SiO₂@Au@TiO₂ photocatalyst (APTES is 3-aminopropyltriethoxysilane). Reprinted with permission from ref. 90. Copyright 2011, Wiley-VCH.

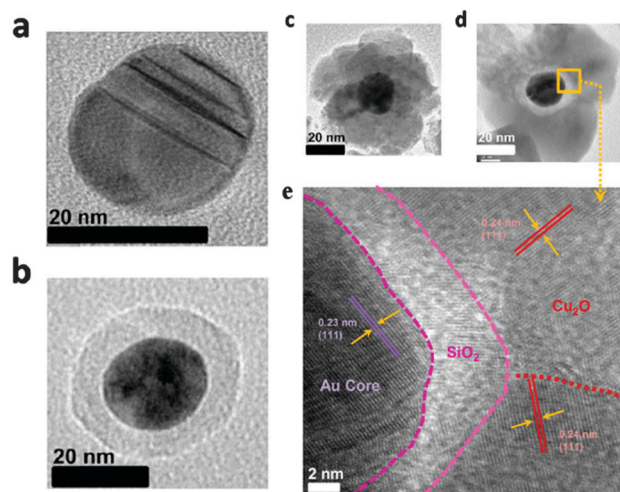


Fig. 6 HRTEM of (a) 20 nm uncoated Au nanospheres, (b) Au@SiO₂ core-shell structure, (c) Au@Cu₂O core-shell structure, (d) Au@SiO₂@Cu₂O sandwich structure and (e) An enlargement of the micrograph for the interface regions of the sandwich structure shows the various crystal orientations. Reprinted with permission from ref. 91. Copyright 2012, American Chemical Society.

Furthermore, a ~25 nm thick Cu₂O layer was also used to coat the Au@SiO₂ core-shell with the hope of creating a Au@SiO₂@Cu₂O sandwich structure, and a higher magnification HRTEM gave the details of the Au@SiO₂@Cu₂O structure confirming the formation of the sandwich structure (Fig. 6e). The LSPRs of these NPs with different structures were also shifted due to a change in the dielectric constant. The bare AuNSs exhibited a broad LSPR centered at 520 nm. However, when coated with the SiO₂ layer, a red-shift of the plasmon peak to 525 nm was observed for Au@SiO₂ core-shell NPs. A further shifted LSPR at 600 nm was also shown in the Au@SiO₂@Cu₂O sandwich structure. The same phenomenon is also apparent for the Au@Cu₂O core-shell NPs, the LSPR of which is 650 nm compared to 620 nm for pure Cu₂O samples.⁹¹ These examples discussed above give directions concerning the synthesis of any kind of efficient Au-based plasmonic photocatalysts for which a precise structural design should be considered in advance, in order to enhance the efficiency of LSPR-dependent light harvesting and charge separation, and finally result in better photocatalytic functions.

3 Recent developments

AuNP-based plasmonic photocatalysts have been recently used to catalyze various chemical reactions at moderate temperatures under UV and visible-light irradiation. Among them, the most important examples are organic transformations and clean energy conversion to develop greener, safer and more effective chemical transformations that are valuable to our environment and society.

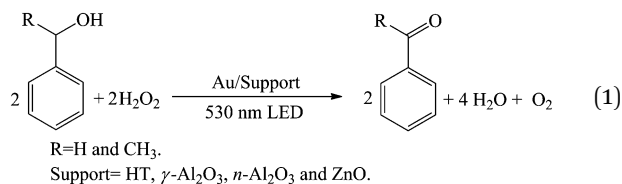
3.1 Organic transformations

In a seminal paper on plasmonic photocatalysis, Awazu *et al.* reported the deposition of TiO₂ on a Ag-SiO₂ core-shell structure.⁸⁵

This plasmonic photocatalyst was very efficient under UV illumination, showing enhancement by a factor of 7 of the decomposition of methylene blue (MB). Chen *et al.*⁵⁶ introduced the SPR effect with a AuNP-based system to catalyze formaldehyde oxidation, which opened the way to organic compound transformations by using AuNP-based plasmonic photocatalysts.

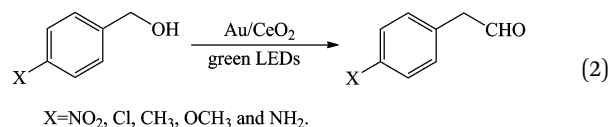
3.1.1 Oxidation of alcohols. Selective oxidation of alcohols by nanogold has been widely investigated as a fundamental organic transformation in both academic laboratories and industry, because carbonyl and carboxylic products serve as important and versatile intermediates in organic synthesis.⁹² Among various alcohol substrates, benzyl alcohol is the most investigated one. Benzyl alcohol has often been used as a reference oxidation reaction to test the catalytic performance of AuNP-based plasmonic photocatalysts.

AuNPs themselves acted as a plasmonic photocatalyst for the oxidation of benzylic alcohols in the presence of H₂O₂ under 530 nm light emitting diode (LED) irradiation as reported by Hallett-Tapley *et al.* This colloidal AuNP plasmonic photocatalyst was found to give high conversion to the corresponding carbonyl products when monochromatic 530 nm LEDs were used. However, recycling the catalyst was unsuccessful.⁹³ To overcome this disadvantage, in later work the authors used AuNPs supported on hydrotalcite and metal oxides (*e.g.*, HT, γ -Al₂O₃, *n*-Al₂O₃ and ZnO) (eqn (1)). It was found that the overall efficiency of alcohol oxidation was strongly dependent on the nature of the support and HT-supported AuNPs resulted in the highest conversion to acetophenone and benzaldehyde from *sec*-phenethyl and benzyl alcohols, respectively, after 40 min of LED irradiation.⁹⁴ Bimetallic nanostructured systems have also been extended to the field of plasmonic photocatalysts. Huang *et al.* synthesized AuPd nanowheels, in which the Au core was surrounded by metallic Pd, by a facile wet-chemical reduction method, and they successfully applied this catalysis system to the oxidation of benzyl alcohol under xenon-lamp irradiation.⁹⁵ Under the same experimental conditions, the introduction of light irradiation promoted faster oxidation with a 97.7% conversion of benzyl alcohol and a 98.0% selectivity in benzaldehyde, compared to 18.4% conversion under the conventional heating within 6 h. This superior light-enhanced catalytic performance is attributed to the unique heterostructure and SPR of the AuPd nanowheels.



However, the monometallic and bimetallic plasmonic photocatalysts suffered from their poor stability under the photocatalytic conditions. To overcome this problem and promote electron-transfer efficiency, various semiconductor-based materials, especially metal oxides (MOs) are used as supports, among which CeO₂, TiO₂ and ZrO₂ are the most used ones. Au/CeO₂ plasmonic photocatalysts prepared by photochemical deposition of HAuCl₄ on CeO₂ in the presence of citric acid as the

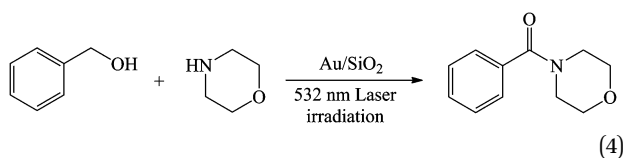
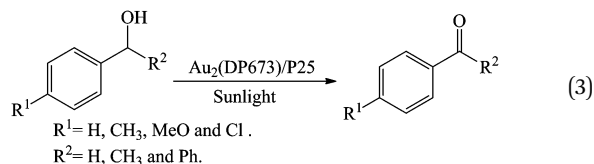
reducing agent showed a maximum SPR absorption at 550 nm.⁹⁶ Under irradiation of green light (530 nm LED irradiation) in the presence of O₂, benzyl alcohol was almost consumed, and benzaldehyde was formed with high selectivity (>99%) in 20 h of reaction time. Other aromatic alcohols and their corresponding aldehydes also showed high conversions and selectivities. It was found that AuNPs with sizes >30 nm were very active under visible light, and the external surface area of the AuNPs played a crucial role in determining the activity of the plasmonic photocatalyst. In order to provide further evidence for this phenomenon, Au/CeO₂ plasmonic photocatalysts prepared by SS and MS photodeposition methods were both shown to be highly efficient in the photocatalytic oxidation of benzyl alcohol under irradiation by green light from a LED (eqn (2)). Benzyl alcohol was completely consumed after 20 h and 15 h for SS-Au/CeO₂ and MS-Au/CeO₂, respectively. In addition, a surprising >99% selectivity to benzaldehyde was also noticeable. It was shown that the external surface area of AuNPs loaded on CeO₂ and the intensity of photoabsorption due to SPR of AuNPs were responsible for the high photocatalytic activity regardless of the type of photodeposition method.²⁴



Various kinds of TiO₂ samples were also used as supports of plasmonic AuNPs. For example, the Au/P25 TiO₂ plasmonic photocatalyst (*d*_{Au} < 5 nm, P25: anatase/rutile ≈ 83/17) was found to be very effective in catalyzing 1-phenylethanol oxidation in toluene under visible light irradiation (λ > 450 nm) compared to its Au/anatase and Au/rutile catalyst counterparts.⁸⁶ More importantly, when the Au₂(DP673)/P25 catalyst was activated by sunlight to catalyze aerobic oxidation of alcohols (eqn (3)), the conversions of alcohols and the corresponding products yields were also greatly enhanced. To further increase the activity and decrease the cost of the catalysts, their recent work showed supported AuNPs that were alloyed with another metal NPs, and this approach to achieve this goal was considered as powerful. For example, AuNPs alloyed with active transition metals like Cu, Pt, Ag and Pd supported on the P25 TiO₂ were successfully synthesized. The results showed that Cu alloying (AuCu/P25) decreased the SPR intensity with a red shift of the band compared with Au/P25 that showed a distinctive SPR band at 551 nm. This led to the enhancement of O₂ activation efficiency and enhanced transfer of plasmon-activated electrons to the oxidized Cu surface atoms, thereby resulting in the best activity in the oxidation of benzylic alcohols under sunlight irradiation at ambient temperature.⁹⁷ In addition, AuNPs alloyed with Pd were also shown to be an efficient plasmonic photocatalyst upon choosing ZrO₂ as the support in the oxidation of benzyl alcohols under visible-light irradiation. The promoting effect was attributed to the distribution of Pd sites and charge heterogeneity at the NP surface.⁸³

Au NPs supported on zeolite also efficiently catalyzed the oxidation of aromatic alcohols to aldehydes under visible light

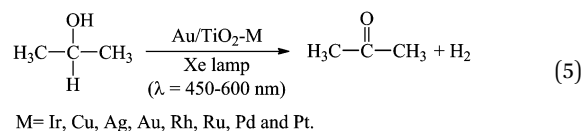
irradiation at ambient temperature.⁹⁸ High product selectivity (>99%) of the photooxidation of benzyl alcohol over Au/zeolite catalysts is noticeable. By comparing the conversion rate of different kinds of alcohols under light and under dark, the authors confirmed that the enhanced photocatalytic ability was related to the LSPR effect of Au NPs. Moreover, the role of molecular oxygen was proved to be the hydrogen remover from the AuNPs surface. Benzyl alcohol was also used as a starting substrate to synthesize amide through a tandem oxidation/amidation process catalyzed by a Au/SiO₂ plasmonic catalyst under 532 nm laser irradiation (eqn (4)).⁹⁹ This proposed reaction was efficient with high conversion and selectivity in the target product and was divided into two continuous steps, in which benzyl alcohol was first oxidized to benzaldehyde. Then, further oxidation of benzaldehyde and morpholine in the presence of H₂O₂ and KOH occurred forming amide in THF.



2-Propanol (IPA) was often used as a substrate for aerobic oxidation to give acetone, the reaction being catalyzed by AuNP-based plasmonic photocatalysts. Liu *et al.* synthesized AuNRs with various aspect ratios supported on TiO₂ and tested their photoactivity by analyzing the amount of acetone and CO₂ under the irradiation of a wide-range visible light.¹⁰⁰ It was shown that the photocatalytic activity was enhanced by 2.8 times in terms of acetone production under broadband light irradiation, which was mainly attributed to the LSPR of AuNR enhancing the broadband visible-light activity. This work provided a simple HClO₄ oxidative method to remove the surfactant that was adhered onto the AuNR surface without noticeably changing its morphology. This strategy is very useful and opens an avenue to develop broadband visible-light sensitive plasmonic photocatalysts, because little work focused on this point. Functionalization of Au/TiO₂ samples with a metal co-catalyst is an effective method for enhancing performances, especially when electron scavenging is important.¹⁰¹ Tanaka *et al.* prepared Au/TiO₂-M (M stands for the metal cocatalyst of Ir, Cu, Ag, Au, Rh, Ru, Pd and Pt) catalysts by a combination of the photodeposition method and colloid photodeposition with a hole scavenger (CPH) method and the formation of H₂ and acetone from 2-propanol over Au/TiO₂-M catalysts under irradiation of visible light from a xenon (Xe) lamp with a Y-48 cut-filter that was used for the model reaction (eqn (5)).¹⁰² The dehydrogenation of 2-propanol occurred stoichiometrically to form H₂ and acetone. The photocatalytic activity of the Au/TiO₂-M samples was found to be highly dependent on the nature of the metal cocatalyst. The best photocatalyst was Au/TiO₂-Pt showing a photocatalytic

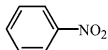
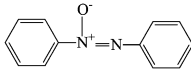
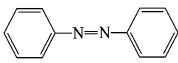
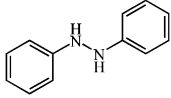
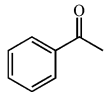
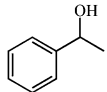
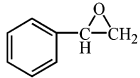
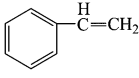
activity that was 5–9 times larger than that of Au/TiO₂ samples. This is due to the fact that the activity of Au/TiO₂-Pt follows a linear relationship with its SPR photoabsorption that is determined by the amount of Au particles. Trilayered nanorod structured plasmonic photocatalysts (Au/Ag/TiO₂) were also synthesized for the photooxidation of 2-propanol visible-light illumination ($\lambda > 420$ nm). The photocatalytic activity of this unconventional structure was strongly dependent on the Au/Ag composition and TiO₂ shell thickness. For example, the activity was increased with increasing Ag content up to Au/Ag = 1 : 5 (molar ratio), then decreased with the further increasing Ag content. A similar phenomenon was also apparent for the increasing thickness of the titania shell. These results related to the photooxidation activity were explained by the cross section of LSPR mediated electron transfer and energy-transfer mechanisms.¹⁰³

The high efficacy of the AuNP-based plasmonic photocatalysts for photoreactions was also evidenced by catalytic oxidation of other alcohols. Examples include aerobic oxidation of 1-phenylethanol to acetophenone on Au-Pd@ZrO₂,^{83,84} oxidation of 4-methoxybenzyl alcohol on Au-Pd@ZrO₂ (ref. 83 and 84) and the Au/Y catalyst,⁹⁸ oxidation of cinnamyl alcohol and 2-phenyl ethanol on the Au/Y catalyst,⁹⁸ oxidation of methanol on Au/TiO₂,¹⁰⁴ and selective oxidation of 4-aminobenzyl alcohol to 4-aminobenzaldehyde (despite the presence of amine functional groups) on Au/CeO₂.²⁴

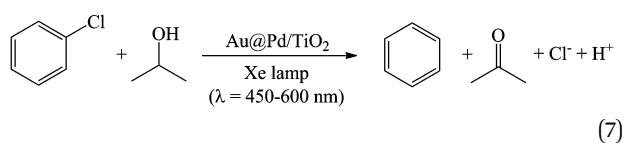
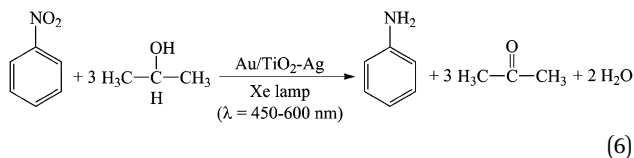


3.1.2 Photocatalytic reduction. In addition to the oxidation reactions discussed above, AuNP-based plasmonic photocatalysts have recently been applied to promote the reduction of organic compounds with high conversion and selectivity under ambient conditions and under visible light. For example, Zhu *et al.* synthesized Au/ZrO₂ catalysts and tested the reaction activity in the reduction of nitroaromatic compounds to form azo compounds under visible or UV-light irradiation.¹⁰⁵ This work highlighted a reduction process driven by sunlight occurring with high selectivity under ambient conditions on Au/ZrO₂ plasmonic photocatalysts. Recently, these authors showed that AuNP/CeO₂ was an efficient photocatalyst for the selective reduction of organic compounds at ambient temperatures under visible-light irradiation.¹⁰⁶ The SPR absorption of AuNPs was found to be crucial for the catalytic activity, and shorter wavelengths led to higher excited-electron energy. Very recently, the supporting effect in the reduction processes on the Au/support (supports: CeO₂, TiO₂, ZrO₂, Al₂O₃ and zeolite Y) was investigated including the reduction of nitro-aromatics to azo compounds, hydrogenation of azobenzene to hydroazobenzene, reduction of ketones to alcohols, and deoxygenation of epoxides to alkenes.¹⁰⁷ Due to the strong linkage between AuNPs and CeO₂, 3 wt% Au/CeO₂ showed the best catalytic performance under the irradiation with visible light (Table 1). The SPR absorption of AuNPs was shown to be crucial for the catalytic activity, and the active Au-H species would react with N=O, N=N and C=O double

Table 1 Performance of 3 wt% Au/CeO₂ in four photocatalytic reductions. (Reprinted with permission from ref. 107. Copyright 2013, Royal Society of Chemistry)

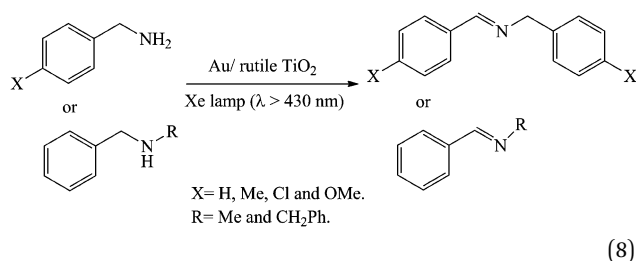
Entry	Reagents	Products	Time (h)	Temp. (°C)	Visible light		No light	
					Conv. (%)	Sel. (%)	Conv. (%)	Sel. (%)
1			2	30	43.5	96	8.1	>99
2			6	30	40	78	10	79
3			24	30	31	>99	1	>99
4			16	25	20	88	4.4	72

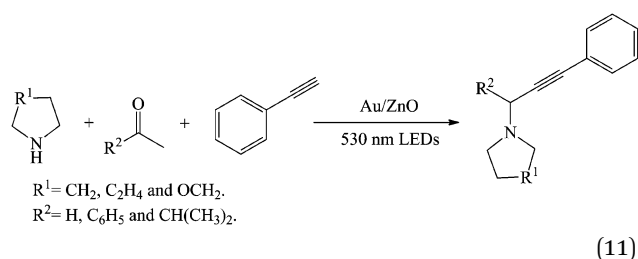
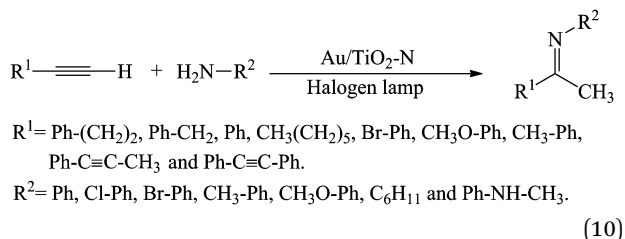
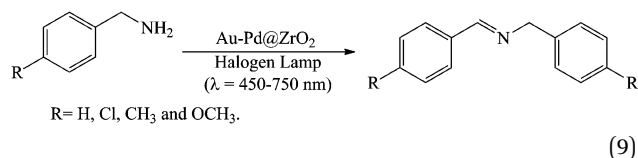
bonds or epoxide bonds depending on the AuNPs excited electrons energy, which can be manipulated by changing the wavelength.^{106,107} Au/TiO₂ plasmonic photocatalysts with a suitable co-catalyst were also found to promote the reduction reactions. A plasmonic Au/TiO₂ photocatalyst with an Ag co-catalyst was shown to be more active than Ag-free Au/TiO₂ in the photocatalytic reduction of nitrobenzene to aniline along with oxidation of 2-propanol to acetone under irradiation of visible light, during which aniline was almost quantitatively formed with a stoichiometric amount of acetone (eqn (6)).¹⁰¹ However, in the case of Au-Pd@ZrO₂ catalyzed reduction of nitrobenzene to azobenzene, the alloyed effect turns out to be negative.⁸³ Functionalization of Au-based plasmonic photocatalysts by formation of a core-shell structure was an effective way to improve the catalytic functions in the photocatalytic reactions. Tanaka *et al.* successfully synthesized core-shell TiO₂-supported Au-Pd nanoparticles (Au@Pd/TiO₂) by using a two-step photodeposition method and introduced the catalysts for the photoreduction of chlorobenzene to benzene along with the oxidation of 2-propanol to acetone under irradiation with visible light (eqn (7)). After irradiation for 20 h, benzene was formed with >99% selectivity at >99% conversion of chlorobenzene, and oxidation of 2-propanol to acetone and H₂ occurred, maintaining the stoichiometry. Both the cocatalyst and SPR effects contributed to improve photocatalytic performances that were optimized by controlling the thickness of the Pd shell.⁸⁸



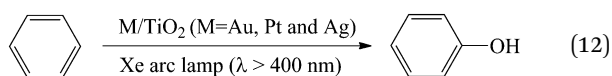
3.1.3 Imine and amine synthesis. Selective aerobic oxidation of amines to imines was also successfully catalyzed by

Au/MOs (MOs stand for metal oxides) plasmonic photocatalysts, in which AuNPs were loaded onto TiO₂, WO₃, ZnO, In₂O₃ and SrTiO₃, under the visible light irradiation ($\lambda > 430 \text{ nm}$) without solvent.¹⁰⁸ Although Au/rutile TiO₂ showed the best catalytic performance with an outstandingly high selectivity (>99%) to imines, the overall conversions of amines were very low (from 0.1 to 4.5%) in a 24 h reaction (eqn (8)). Moreover, the AuNP size effect was also a determining factor, because the increase in AuNP size led to the increases in LSPR absorption intensity while decreasing the AuNP surface area. Thus, the optimum diameter of the AuNPs is about 6.7 nm resulting in the best photocatalytic activity. In the case of Au-Pd/ZrO₂ catalysts,⁸³ the activity of catalytic oxidation of benzylamine into imines is greatly enhanced upon visible-light irradiation in CH₃CN solvent (eqn (9)). In addition, the target product, imine, can also be obtained by hydroamination of alkynes with anilines on an Au/TiO₂-N (AuNPs supported on nitrogen-doped TiO₂ nanofibres) plasmonic photocatalyst with toluene as the solvent under visible-light irradiation (eqn (10)).¹⁰⁹ The reaction was achieved in high yield and selectivity. Interestingly, the supporting effect was more important than the size effect to render the photocatalyst active or inactive due to the presence of Ti³⁺ in nitrogen-doping TiO₂ that enhanced the conversion without sacrificing the selectivity. Similarly, one-pot synthesis of propargyl amines by ternary coupling of aldehyde, alkyne and secondary amine was successfully performed using the Au/ZnO catalyst under 530 nm LED irradiation (eqn (11)), which led to the rapid and selective formation of these products in good yields under ambient conditions.¹¹⁰





3.1.4 Hydroxylation of benzene to phenol. The one-step hydroxylation of benzene to phenol is challenging, because this reaction usually gives low yield and selectivity. Introducing plasmonic photocatalysts to catalyze benzene hydroxylation might provide a valuable solution to solve this problem. Zheng *et al.* synthesized noble-metal plasmonic photocatalysts M@TiO₂ (M = Pt, Ag and Au) by a facile *in situ* method and tested the photocatalytic performance under visible light ($\lambda > 400$ nm) (eqn (12)). Among these three kinds of catalysts, Au@TiO₂ showed the best results. The content of Au loading was a key factor in determining the photocatalytic activity and selectivity. 2 wt% Au loading showed the best dispersivity and photocatalytic performance with 63% yield and 91% selectivity, which may be attributed to the enhanced visible light absorption as well as the strongest SPR effect.⁸⁹ The sunlight-introduced photocatalytic oxidation of aqueous hydroxylation of benzene on Au@TiO₂ was considerably improved when the reaction atmosphere was CO₂. A CO₂ effect was noticed and 13% yield and 89% selectivity for phenol were obtained on 3% Au/P25 under 230 kPa of CO₂, which is of environmental interest.¹¹¹



3.1.5 Decomposition/degradation of organic compounds. Photocatalytic decomposition of volatile organic compounds (VOCs) and purification of the environment on the basis of AuNP-based plasmonic photocatalysts have also attracted increasing attention. Hou *et al.* synthesized a Au/TiO₂ plasmonic photocatalyst by depositing ~5 nm AuNPs on the TiO₂ surface and tested its photocatalytic activity in methyl orange (MO) photodecomposition under visible illumination. A more than 9-fold improvement in the photocatalytic decomposition

rate of MO on the Au/TiO₂ plasmonic photocatalyst was highlighted.¹¹²

Engineering of AuNPs or TiO₂ with appropriate morphologies and dominant facets contributed to the enhancement of the design of high-performance photocatalysts. As reported, titania-coated 2D array AuNP photocatalysts were fabricated by wet chemical bottom-up deposition processes. Due to the LSPR peak of the AuNP 2D array at around 700 nm with a full-width at half-maximum of 350 nm, a 6.5 times higher photodegradation rate was confirmed compared to the titania reference sample under visible light irradiation.¹¹³ The cuplike anatase TiO₂ crystals with mesoporous structure decorated with plasmonic AuNPs were synthesized using a very facile silica template method and chemical etching treatment. Compared with the AuNPs modified TiO₂ hollow spheres (HSSs) and P25 TiO₂, the Au/TiO₂ nanocup showed the highest reaction rate of decomposition of MB under visible light irradiation (780 nm $\geq \lambda \geq$ 400 nm). The photocatalytic activity follows an order of Au-TiO₂ nanocups > Au-TiO₂ HSSs > Au-P25 > TiO₂ nanocups and TiO₂ HSSs that is attributed the unique structure of TiO₂ nanocups and the LSPR effect of AuNPs.¹¹⁴ An enhancement of photocatalytic activity was also obtained by increasing the percentage of TiO₂{001} facets. AuNPs with an average diameter of *ca.* 5 nm were deposited on the {001} facet of TiO₂ nanosheets in the form of a Au/TiO₂ plasmonic photocatalyst, and this nanomaterial showed superior photocatalytic activities toward the degradation of rhodamine B (RhB) in aqueous solution. The possible mechanism is illustrated as follows (Fig. 7): (1) under visible light irradiation, the SPR effect of AuNPs on the TiO₂-001 surface promoted electron transfer between them. (2) Photodegradation of RhB would start from hole (*Au⁺) attack. Meanwhile, oxygen trapped electrons to form *O₂⁻ radicals that react with H⁺ and trapped electrons to produce H₂O₂ in aqueous solution. (2) RhB was destroyed *via* the formation of *O₂⁻ and *OH radicals. Additionally, when the reaction does not involve O₂, h⁺ played a predominant role rather than *O₂⁻ and *OH radicals under visible-light irradiation.¹¹⁵

The high-yield, well-dispersed and tightly-interacted AuNP/titanate nanobelt heterojunctions are also found to possess high photocatalytic activity in the MO photodecomposition reaction. AuNP/titanate nanobelt heterojunctions self-assembled with

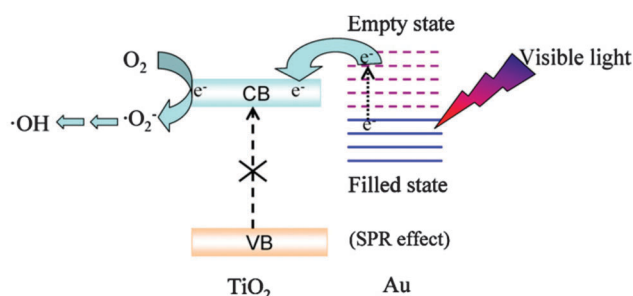


Fig. 7 The possible mechanism for photocatalytic degradation of RhB over AuNP/TiO₂-001. Reprinted with permission from ref. 115. Copyright 2012, Elsevier B.V.

the linker molecule of thioglycolic acid were prepared by Liu *et al.*¹¹⁶ It was shown that the activity for MO photodegradation depended on the content of the Au precursor, and 5 wt% Au nanocrystals showed the best degradation ratio under visible-light irradiation due to the SPR excitation of Au nanocrystals. The photodegradation of MO on the AuNP/TiO₂ nanocomposite also proved to be of high efficiency under sunlight irradiation. Naik *et al.* introduced a green method to synthesize the AuNP/TiO₂ nanocomposite; all the AuNP/TiO₂ samples showed better efficiency towards photodegradation of MO than neat TiO₂, because the SPR effect determined the electron-transfer efficiency between AuNPs and TiO₂ in the presence of solar-light irradiation. In addition, the photocatalytic activity was also found to be strongly affected by pH and plant-extract concentration. More importantly, the rate of MO degradation over AuNP/TiO₂ followed first-order kinetics.¹¹⁷ More recently, AuNPs deposited on anatase TiO₂ mesocrystal (Au/MesoTiO₂) superstructures showed a more than 10 times activity in liquid-phase visible-light photocatalytic degradation of MB than that of Au/NanoTiO₂ and Au/P25 systems (Fig. 8a). This was mainly induced by the SPR excitation of the AuNPs; the mechanism of this activation is discussed in Section 4.1.¹¹⁸ Photocatalytic decomposition reactions are also promoted when semiconductor catalysts are decorated with metal NP arrays. Kochuveedu *et al.* reported SiO₂@TiO₂ core-shell nanospheres decorated with AuNP arrays at high densities for methylene blue (MB), MO and *p*-nitrophenol (PNP) photodegradation under visible light. This plasmonic AuNPs decorated SiO₂@TiO₂ (SiO₂@TiO₂-Au) showed stable and recyclable visible-light photocatalytic efficiency because the optimum size and density of AuNPs on the surface of TiO₂ determined the synergistic effect between Au NPs and TiO₂ and the SPR excitation degree.¹¹⁹ In contrast, when AuNPs coated with SiO₂ were supported on TiO₂, namely with the shell-isolated plasmonic photocatalyst (Au@SiO₂/TiO₂), higher MB photodegradation efficiency was obtained than that of Au/TiO₂ under both UV and visible-light irradiation in 5 h, because its LSPR was much higher.¹²⁰

The combination of one-dimensional (1D) anisotropic nanostructured semiconductor materials such as KNBO₃ nanowires (NWs) and TiO₂ nanotubes (NTs) with plasmonic metal NPs

showed great promise in plasmonic photocatalysis of degradation reactions. As a wide-band-gap semiconductor material, 1D KNBO₃ nanowires modified with AuNPs showed high performance in photocatalytic degradation of RhB reaction, as reported by Lan *et al.*¹²¹ This work suggested that photocatalytic reactivity can be tuned by changing the 1D anisotropic nanostructures and the AuNP size. In the case of depositing AuNPs on the 1D TiO₂NTs through a DP process followed by calcination, a homogeneous distribution of AuNPs on both internal and external tube-walls of TiO₂ NTs was obtained and they served as an efficient plasmonic photocatalyst in the decomposition of MB at room temperature. Under visible-light irradiation, the SPR absorption from the AuNPs surface increased, enhancing the separation of e⁻-h⁺ charge pairs at the interface of the mixed TiO₂ NTs, which resulted in the enhancement of photocatalytic efficiency of Au/TiO₂ NTs compared to TiO₂ NTs without AuNP deposition.¹²²

Visible-light photodegradation of organic compounds on unconventional structured catalysts such as core-shell and sandwich nanostructures has also been reported. In the case of Au@ZnO core-shell NP-catalyzed photodegradation of MO dyes and photooxidation of methanol under visible irradiation, Misra *et al.* concluded that Au@ZnO core-shell NPs exhibited efficient plasmonic photocatalytic activity because of the presence of SPR of the Au core; the photocatalytic activity was enhanced with an increase in shell thickness.¹²³ In contrast, SiO₂/Au/TiO₂ sandwich-structured catalysts showed high efficiency in catalyzing decomposition of organic compounds under illumination of UV, visible light and natural sunlight, which can be ascribed to interfacial nonmetal doping-improved visible-light activity. AuNP decoration enhanced light harvesting and charge separation, and the small grain size of anatase nanocrystals reduced the exciton recombination rate.⁹⁰ Pure Au, Cu₂O, Au@Cu₂O core-shell and Au@SiO₂@Cu₂O sandwich NPs were also introduced for the photodegradation of MO in aqueous solution under visible light (Fig. 8b). Among these three catalysts, Au@SiO₂@Cu₂O sandwich NPs exhibited the best photocatalytic activity, and enhanced photocatalytic activity at the LSPR wavelengths was attributed to an interaction between the LSPR and semiconductor through the local electromagnetic field dominated by the resonant energy transfer (RET) mechanism.⁹¹

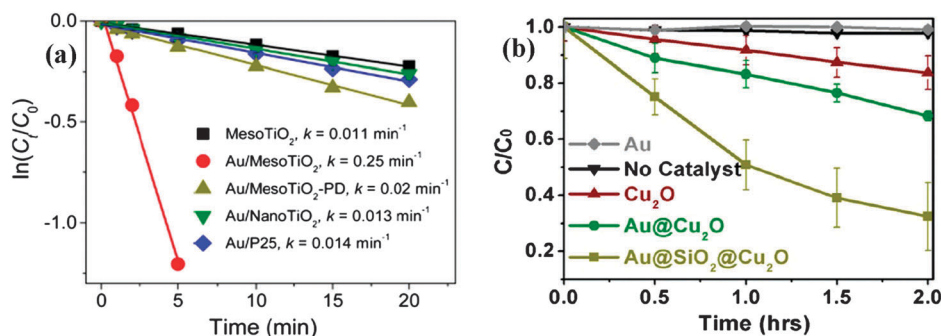


Fig. 8 (a) Kinetic linear fitting curves for liquid-phase photocatalytic degradation of MB over different samples under visible-light irradiation (460–700 nm), and (b) no catalyst, uncoated Au, Cu₂O control, Au@Cu₂O, and Au@SiO₂@Cu₂O nanostructures. Reprinted with permission from ref. 118 and 91. Copyright 2012–2013, American Chemical Society.

Apart from the examples discussed above, the AuNP-loaded rutile TiO_2 (Au/rutile TiO_2) plasmonic photocatalyst successfully extended its application to water purification, which involved rapid and complete removal of nonylphenol from its dilute aqueous solution by degradation.¹²⁴ And, Au/ TiO_2 prepared by the CPH method was also used for the photodecomposition of oxalic acid and acetic acid to CO_2 as well as formic acid under visible light irradiation.¹²⁵ Moreover, plasmon-enhanced photocatalytic decomposition was also tested by using other organic compounds like trichloroethylene (TCE). By choosing nonporous SiO_2 nanospheres as an inactive support to prevent NP coalescence or sintering, and depositing on 5 nm AuNPs, higher reaction rates by manipulating the wavelength of the incident light with the plasmon resonance of the catalysts (532 nm) were obtained.¹²⁶ All these results promoted an advanced, non-toxic, low-cost, and easy photocatalytic process for water purification.

3.1.6 Miyaura–Suzuki coupling reactions. The Miyaura–Suzuki coupling reaction has greatly contributed to the straightforward and convenient synthesis of biaryls in organic synthesis. Great efforts have been made to use transition metals to catalyze Miyaura–Suzuki coupling reactions, especially using homogeneous palladium catalysts. Very recently, the interest in palladium catalysts has shifted to bimetallic AuPd plasmonic photocatalysts, especially under ambient conditions, which is promising for practical and industrial applications. Wang *et al.* reported plasmonic harvesting of light energy for Miyaura–Suzuki coupling reactions under laser and solar irradiation on Au–Pd nanostructures, with PdNPs that were grown on the surface of AuNRs (eqn (13)).¹²⁷ It has been demonstrated that light was absorbed by the Au nanocrystal cores and that PdNPs promoted the Suzuki coupling reactions, with the smaller Au–Pd nanorods showing the best photocatalytic performance. More importantly, the high catalytic activity is mainly attributed to the plasmonic photocatalysis contribution rather than photothermal heating contribution, which was confirmed by comparing the activities of Au–Pd and Au– TiO_x –Pd catalysts. That is, the Au– TiO_x –Pd catalysts possessed only the photothermal heating effect while the Au–Pd nanorods showed both the plasmonic photocatalysis and the photothermal heating effects for the Miyaura–Suzuki coupling reactions. Unconventional structures containing bimetallic AuPd nanowheels were synthesized by a facile wet-chemical reduction method in which the AuNP core was surrounded by metallic Pd that also acted as a highly efficient catalyst in Miyaura–Suzuki coupling reactions under light irradiation, which could be attributed to the unique heterostructure and SPR of AuPd nanowheels.⁹⁵ When alloyed Au–Pd NPs supported on ZrO_2 (Au–Pd@ ZrO_2) were tested for the Miyaura–Suzuki coupling reaction under visible-light illumination (eqn (14)), high yields of the target products were obtained, because the activation energy of Miyaura–Suzuki coupling was reduced to $\sim 33.7 \text{ kJ mol}^{-1}$ compared to $\sim 49.2 \text{ kJ mol}^{-1}$ in the dark.⁸³

A discussion of whether the enhancement of the chemical reaction is attributed to contributions of the light or thermal effect is necessary, because irradiation causes increase of the

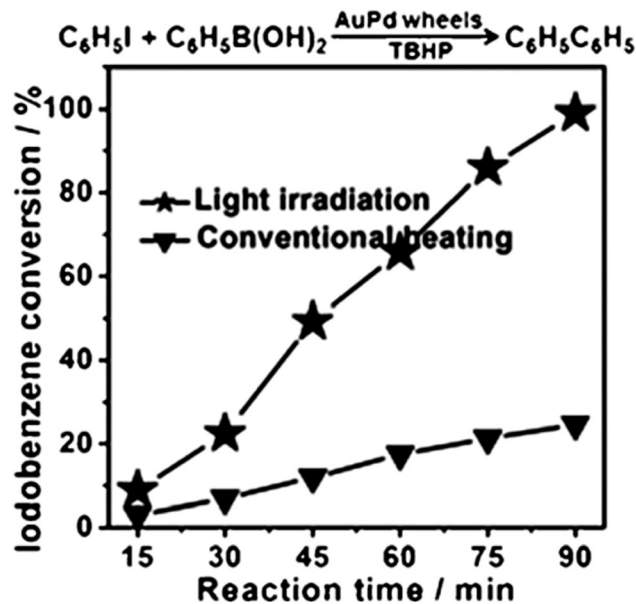
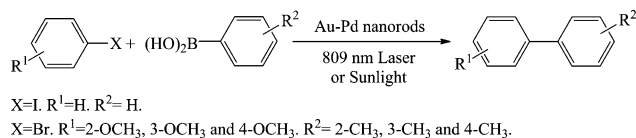
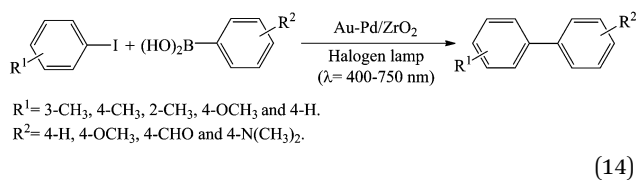


Fig. 9 Conversion of iodobenzene as a function of time during a Miyaura–Suzuki coupling reaction under irradiation with light or conventional heating conditions. Reprinted with permission from ref. 95. Copyright 2012, Wiley–VCH.

reaction temperature.¹²⁷ By comparing the activity under light irradiation and conventional heating conditions (photocatalytic activity of the former is 3.8 times greater than that of the later), the AuPd nanowheels enhanced not only the catalytic activity but also their ability to exploit the light (Fig. 9). Further study on the dependence of the catalysis on the reaction temperature and light intensity confirmed that the accelerated rate of the reactions under light irradiation was due to the plasmonic resonance effect, which inspired the design of new catalyst systems for chemical conversion reactions under ambient conditions. In the case of Au–Pd@ ZrO_2 -catalyzed Miyaura–Suzuki coupling,⁸³ Sarina *et al.* discussed contributions of light and thermal processes to the conversion efficiencies in detail by tuning the light intensity and wavelength. As shown in Fig. 10a, the linear relationship between the conversion and the light intensity clearly demonstrated the enhancement that light irradiation produced in the catalytic activity of Au–Pd@ ZrO_2 catalysts. More importantly, in the longer light-wavelength range (especially the LSPR peak of AuNPs is in this wavelength), the contribution of light is superior to that of the thermal effect, Fig. 10b. These results clearly demonstrated that the enhancement of photocatalytic activity is mainly attributed to light-excited plasmonic photocatalysis, which inspires the design and usage of combined gold and other transition metals as efficient catalysts for a wide range of organic synthesis reactions promoted by sunlight.



(13)



In short, the transformation of organic starting materials to target compounds in a green, effective and low-cost process is always a pursuit, especially under ambient conditions. Although rapid progress has been made in the area of organic transformations by AuNP-based plasmonic photocatalysts under visible light irradiation, the reactions types catalyzed by these promising photocatalysts are still limited. Great efforts are still needed to continue understanding plasmonic gold-photocatalyzed organic reactions from both fundamental and mechanistic points of view in order to guide the design of catalysts and extend the reaction types.

3.2 Clean energy conversion

3.2.1 Water splitting. With the understanding of the exhaustion of fossil fuels and the deterioration of ecological environment, scientists are encouraged to develop clean and renewable energies. Among them, hydrogen (H_2) is considered as the simplest and most attractive fuel for production due to its high-energy capacity and friendly environment. Utilization of solar energy to produce hydrogen as a storable clean fuel using sunlight to drive a photocatalytic or photoelectrochemical (PEC) water splitting reaction producing H_2 and oxygen (O_2) is attractive. Since the first report of the use of a plasmonic photocatalyst to split water in a plasmon-enhanced photocurrent generation system,¹²⁸ considerable advances¹²⁹ have been made in solar-to-hydrogen energy conversion *via* plasmonic photocatalysis, and research is still in progress.

In a study by Liu, photocatalytic water splitting was investigated under visible illumination in TiO_2 film by exploiting the large plasmon resonance of AuNPs. Compared to TiO_2 with no AuNPs, a significant enhancement factor of 66 was highlighted for the photocurrent value with AuNPs at $\lambda = 633$ nm (Fig. 11). The LSPR contributes to the enhancement in the photocatalytic splitting of water in the visible region due to the electromagnetic spectrum photocurrent value that increases at the plasmon

resonant wavelength.¹²⁸ This represents a possible route to direct solar energy to fuel production using plasmonic photocatalysts, which was further supported by Chen *et al.* These authors suggested that AuNPs not only acted as electron traps as well as active sites but also played an important role in the SPR enhancement to provide extra electromagnetic field for the enhancement of H_2 production in photocatalytic water splitting.¹³⁰ However, a comparison of the photoelectrochemical water splitting performance over Ag/N- TiO_2 and Au/N- TiO_2 also suggested that the Au SPR is insufficient to lead to the formation of $e^- - h^+$ pairs in N- TiO_2 in the radiative energy transfer process, because N- TiO_2 absorbs only below ~ 500 nm.⁵⁷ More recently, an efficient, autonomous plasmon-enhanced solar water splitting device based on a AuNR array was reported by Moskovits' group. The AuNRs were first coated with a thin TiO_2 layer for charge separation. Then, the TiO_2 was covered by tiny Pt NPs that capture the hot electrons and thereby trigger the reduction of hydrogen ions. Moreover, a cobalt based catalyst was used to feed the metal back with electrons. All effective charge carriers involved in the oxidation and reduction steps arise from the hot electrons resulting from the excitation of surface plasmons in the AuNRs. The as-reported AuNRs function without external wiring, producing 5×10^{13} H_2 molecules per cm^2 per s under 1 sun illumination (AM 1.5 and 100 mW cm^{-2}) with unprecedented long-term operational stability.¹³¹

As already illustrated in 1.2.2, the NP shape plays a major role in determining the SPR absorption peak, resulting in various catalytic functions. Thus, the photoactivity of Au- TiO_2 electrodes for photoelectrochemical water oxidation is effectively enhanced in the entire UV-visible region by tuning the shape of AuNPs. For example, depositing AuNPs, AuNRs and a mixture of AuNPs and AuNRs on the surface of TiO_2 nanowire arrays as photoanodes for photoelectrochemical water oxidation enhances the photoactivity of TiO_2 at various wavelengths. An electric-field amplification effect was observed for AuNP- TiO_2 due to electric-field increase at wavelengths between 300 and 400 nm (overlapped with the absorption edge of TiO_2), which together with the effective surface passivation promoted water oxidation in the UV region. Most importantly, the electrical-field amplification effect and hot-electron generation upon SPR excitation are responsible for

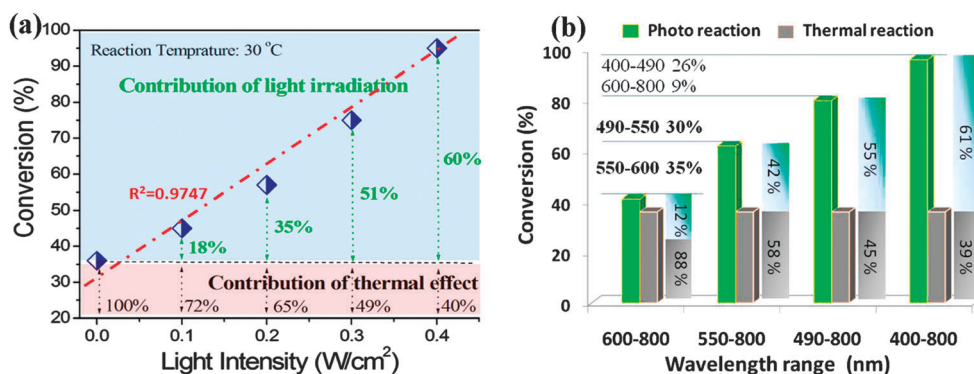


Fig. 10 Dependence of the catalytic activity of Au-Pd@ZnO₂ catalysts for the Miyaura-Suzuki coupling reaction on (a) intensity and (b) wavelength of light irradiation. Reprinted with permission from ref. 83. Copyright 2013, American Chemical Society.

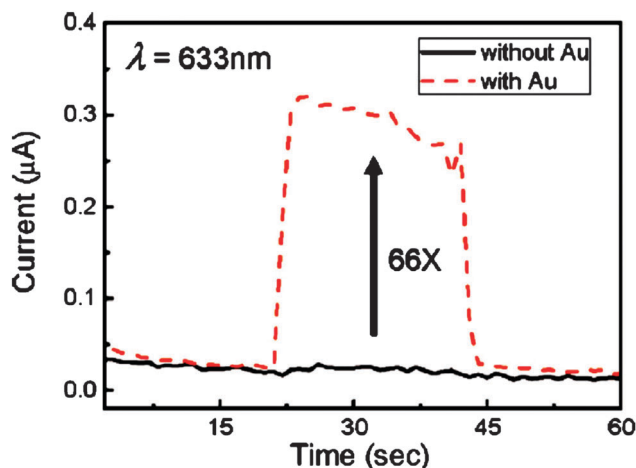


Fig. 11 I - V characteristics of anodic TiO_2 with and without AuNPs irradiated with $\lambda = 633$ nm light for 22 s. Reprinted with permission from ref. 128. Copyright 2011, American Chemical Society.

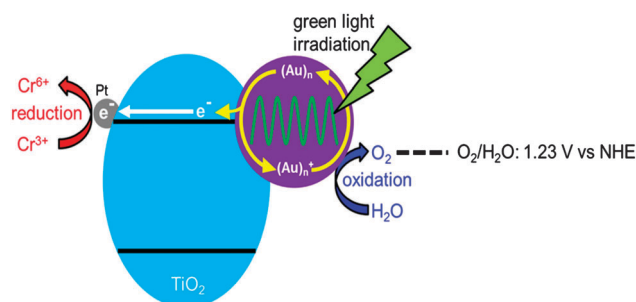
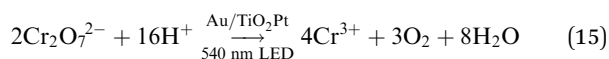


Fig. 12 Expected working mechanism for the reduction of Cr^{6+} to Cr^{3+} along with H_2O oxidation to O_2 over Au/TiO_2 -Pt under irradiation with visible light. Reprinted with permission from ref. 133. Copyright 2013, American Chemical Society.

the photoactivity enhancement over Au nanostructure-decorated TiO_2 samples in the visible region.¹³² Furthermore, as also described in 3.1.1, the addition of a suitable metal co-catalyst with Au/TiO_2 effectively promotes alcohol oxidation reactions, and so does it in the H_2O oxidation reaction. The Au/TiO_2 -Pt photocatalysts were successfully applied to Cr^{6+} reduction and H_2O oxidation reactions under the visible-light irradiation of a green LED ($\lambda = 540$ nm) (eqn (15)). The proposed mechanism of this reaction is illustrated in Fig. 12. To begin with, AuNPs are excited by SPR under visible-light irradiation and absorb the incident photons. Then, electrons are transferred from AuNPs to the conduction band of TiO_2 . Finally, the resultant electron-deficient AuNPs oxidize H_2O to O_2 and return to the original metallic state, while Cr^{6+} is reduced to Cr^{3+} , because electrons are transferred from the TiO_2 conduction band to PtNPs. This reaction does not induce irreversible changes in the photoabsorption property and activity of the photocatalysts.¹³³



Metal-semiconductor hybrid photocatalysts were shown to be efficient in solar H_2 production. For instance, mesoporous $\text{Au}-\text{TiO}_2$ nanocomposites showed remarkable visible-light activity for H_2 evolution from photocatalytic water reduction in the presence of ascorbic acid as the electron donor, which can be explained the defects/impurity states in the TiO_2 matrix; the AuNP LSPR enhanced the weak visible-light excitation of the TiO_2 matrix.¹³⁴ On the other hand, by arranging plasmonically modified wide-bandgap oxides in three dimensions (3D), visible-light-active electrochemical water-splitting photocatalysts are also obtained. DeSario *et al.* prepared 3D $\text{Au}-\text{TiO}_2$ aerogels using the sol-gel procedure and deposited AuNPs onto anatase TiO_2 aerogels (DP $\text{Au}-\text{TiO}_2$) as catalysts for comparison.¹³⁵ Various preparation methods lead to almost the same average AuNP size that is 4.7 ± 1.5 nm and 4.7 ± 1.9 nm for the DP-8.5% and 3D-8.5% samples, respectively. However, the SPR absorptions are quite different from one another. The SPR in DP Au/TiO_2 markedly red-shifts by 20–25 nm relative to that of 3D $\text{Au}-\text{TiO}_2$ aerogels that is centered at 545–548 nm and shows the maximum improvement factor of 55 in visible-light photoactivity. Another example also demonstrated that the use of an ultrathin layer of a suitably chosen material to coat a light-harvesting nanostructure helps enhancing the benefits of AuNP near-field plasmonic functionalization in the context of photoelectrochemical water splitting.¹³⁶ The $\text{Au}/\text{ZFO}/\text{ZnO}$ nanocomposites are prepared by first depositing ZnFe_2O_4 (ZFO) onto ZnO nanorods followed by a second deposition of AuNPs onto the ZFO/ZnO nanostructure. UV-visible absorption spectra showed that $\text{Au}/\text{ZFO}/\text{ZnO}$ had the highest absorption in the visible region. Furthermore, due to the near-field optical enhancement effect of plasmonic AuNPs on ZFO/ZnO nanostructured hetero-junction, the photocurrent densities of $\text{Au}/\text{ZFO}/\text{ZnO}$ are five times and two times higher than that for ZnO and ZFO/ZnO samples, respectively. These examples highlight the importance of the material design when considering the use of plasmonic photocatalysts under visible light based on LSPR as already discussed in 2.3 and 3.1.5.

3.2.2 H_2 formation from organic compounds. H_2 formation by nanogold plasmonic photocatalysts from organic compounds (or organic–water mixture) has also attracted much attention. Tanaka *et al.* showed that catalyst preparation methods greatly influence the H_2 formation rate from organic compounds. The Au/TiO_2 catalysts were synthesized by SS and MS photodeposition methods. A larger rate of photoinduced H_2 production from various substrates (2-propanol, ethanol, methanol, ammonia and benzyl alcohol) was reported under irradiation using visible light. MS- Au/TiO_2 samples exhibited the highest H_2 formation rate. Indeed, the SPR of AuNPs exhibited stronger photoabsorption at around 550 nm.¹³⁷ Very recently, these authors also suggested that the co-existence of large (>10 nm) and small (<5 nm) AuNPs in Au/TiO_2 catalysis prepared by MS photodeposition method contributed to stronger SPR photoabsorption, enhanced H_2 evolution rate from 2-propanol in aqueous suspensions, and H_2 and N_2 evolution rates from NH_3 under visible light irradiation. In these cases, smaller AuNPs acted as a reduction site for H_2 evolution. However, in the case of the mineralization of acetic acid in the presence of O_2 , smaller Au

particles had little effect on the photoactivity, because O_2 itself acting as the electron acceptor is enough for reduction of electrons from CB of TiO_2 . Thus, controlling electron consumption is an effective way for nanogold based plasmonic photocatalysts to improve photocatalytic performance.⁸⁹ The AuNP loading effect is also important for the H_2 production from ethanol–water mixtures under UV excitation.¹³⁸ By loading 0–10 wt% AuNPs on the P25 TiO_2 , highest activities were observed in the Au loading range 0.5–2 wt% (H_2 production rate 31–34 mmol g⁻¹ h⁻¹), because in this range of Au loading, LSPR excited AuNPs effectively suppress electron–hole pair recombination in TiO_2 to promote H_2 production. The size effect of AuNPs is ignored in this case, because all samples had almost the same average AuNP diameter. Normally, the AuNP size effect has a great influence on the photocatalytic performance. This was shown in the case of Au-loaded mesoporous Ta_2O_5 (Au/m- Ta_2O_5 plasmonic photocatalysts) prepared by a facile photodeposition method. The larger size of AuNPs led to a stronger SPR effect thereby resulting in the enhancement in the photocatalytic H_2 production rate from methanol aqueous solution.¹³⁹

The electron-transfer pathway in Au/ TiO_2 is essential to understand the underlying mechanism of the SPR absorption as well as its impact on the H_2 production reaction. Using *in situ* electron paramagnetic resonance (EPR) spectroscopy, Priebe *et al.* investigated the visible-light-driven electron transfer in photocatalytic H_2 evolution from MeOH– H_2O mixtures over Au– TiO_2 catalysts.¹⁴⁰ Their work suggested that the electron-transfer pathways are dependent on the wavelength of the light, namely, e^- – h^+ pair generation by d–sp interband transition in the shorter wavelength region, while the electron-transfer pathway in the higher wavelength range of the visible spectrum is dependent on SPR transitions. Furthermore, synergistic promotion of the photocatalytic activity of TiO_2 by AuNP deposition under UV-visible light irradiation was also observed.¹⁴¹ As shown in Fig. 13, upon visible-light irradiation, electrons in large AuNPs are excited by LSPR and transferred to the conduction band of adjacent TiO_2 , during which the local electric field of adjacent TiO_2 and separation of electron–hole pairs are enhanced. Meanwhile, small AuNPs on TiO_2 act as efficient co-catalysts and trap the electrons from the conduction band of TiO_2 . Thus, a triple synergistic promotion effect is achieved in the separation of electron–hole pairs over TiO_2 by large and small AuNP deposition. This was proved by Rayalu *et al.* who deposited AuNPs on TiO_2 by a photodeposition method, showing that the highest H_2 evolution rate under visible-light irradiation was because of the formation of the plasmonic state of AuNPs upon illumination with the light source.²⁵

A higher performance also benefited from the successfully nanostructure design. Janus Au– TiO_2 photocatalysts (Fig. 14b inset)¹⁴² were rarely explored compared to their core-shell counterparts, the LSPR properties of which have been widely studied.^{81,91,119} However, the Janus morphology generates extremely strong localization of the plasmonic near-field close to the Au– TiO_2 interface, leading to the enhancement of optical absorption and the generation of e^- – h^+ pairs for photocatalysis and resulting in a higher H_2 generation rate from isopropyl

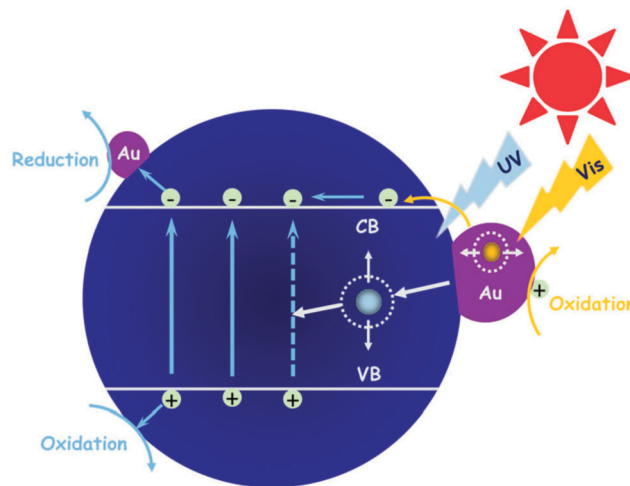


Fig. 13 Synergistic promotion effects of AuNPs on the photocatalytic activity of TiO_2 under UV-visible light irradiation. Reprinted with permission from ref. 141. Copyright 2013, Royal Society of Chemistry.

alcohol–aqueous solution (Fig. 14a). The size effect is also clearly seen in this novel nanostructured photocatalysis. Under visible-light irradiation, the rate of H_2 generation from the Janus photocatalysts decreased in the order: $Au_{70nm}-TiO_2 > Au_{50nm}-TiO_2 > Au_{30nm}-TiO_2$, suggesting that larger AuNPs resulted in higher photocatalytic activity, which was ascribed to their stronger plasmonic near-fields (Fig. 14b). Torimoto *et al.* prepared a novel semiconductor/insulator/metal structured hybrid photocatalyst ($CdS@SiO_2//Au@SiO_2$) composed of AuNPs and CdSNPs, separated by an insulating SiO_2 layer, as shown in Fig. 15a, for H_2 production from 2-propanol–water. In this nanocomposite catalyst, the AuNP core acts as light capture and the local electric field around AuNP cores is enhanced *via* LSPR, while the SiO_2 layer works as an insulator layer to prevent direct electron transfer from CdS to AuNPs. Fig. 15b shows the amount of H_2 as a function of irradiation time over $CdS@SiO_2$ and $CdS@SiO_2//Au@SiO_2$ catalysts with various SiO_2 shell thicknesses. The photocatalytic activity of the $CdS@SiO_2//Au@SiO_2$ catalyst

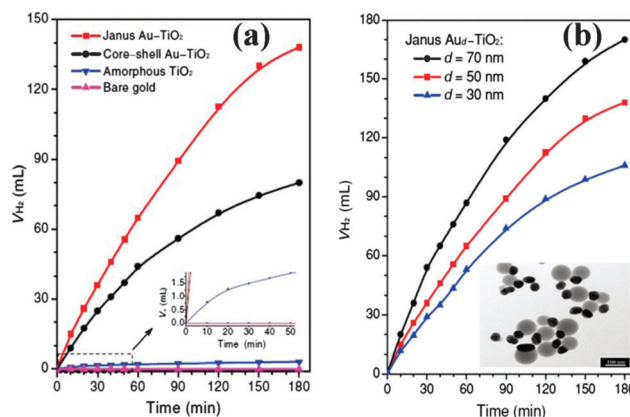


Fig. 14 (a) Volume of hydrogen generated (V_{H_2}) under visible-light irradiation using various nanostructures (AuNP size: 50 nm) and (b) Janus Au_d-TiO_2 photocatalysts with various AuNP sizes d (in nm). Reprinted with permission from ref. 142. Copyright 2012, WILEY-VCH.

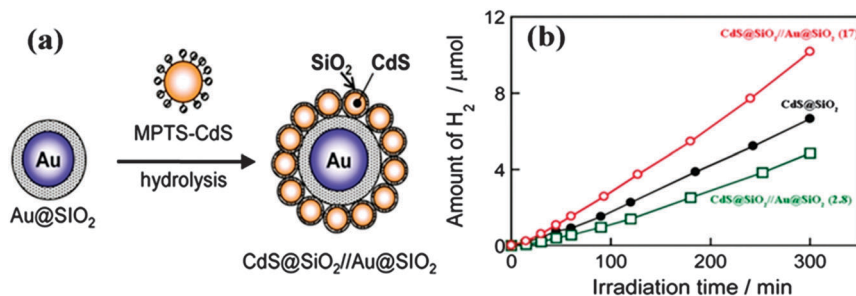
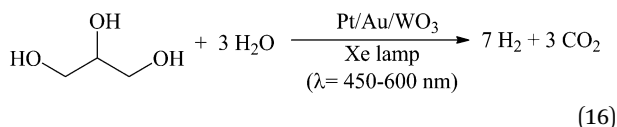


Fig. 15 (a) Schematic illustration of the immobilization of CdS@SiO₂ on Au@SiO₂ particles. (b) Amount of H₂ evolved as a function of irradiation time over CdS@SiO₂//Au@SiO₂ photocatalysts ((17) and (2.8) mean thickness of the SiO₂ shell layer in CdS@SiO₂//Au@SiO₂ samples is 17 and 2.8 nm, respectively). Reprinted with permission from ref. 143. Copyright 2011, American Chemical Society.

with a SiO₂ shell thickness of 17 nm is higher than that of CdS@SiO₂//Au@SiO₂ with an SiO₂ shell thickness of 2.8 nm, suggesting that the photocatalytic activity is dependent on the distance between the cores of the CdSNPs and AuNPs, which can also be tuned by changing the AuNP core size.¹⁴³

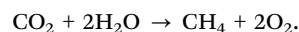
Combining plasmonic photocatalysts and band-gap photocatalysts (Pt/Au/WO₃) has been recently shown to be a powerful method for the photocatalytic decomposition of glycerin, a byproduct in the production of soap and biodiesel oil from fats and oils. This reaction leads to the formation of H₂ and CO₂ under visible light irradiation (eqn (16)). A study of H₂ production from 2-propanol under additional irradiation by light from the blue LED or green LED indicated that both the band-gap excitation of WO₃ and SPR of AuNPs simultaneously contributed to the H₂ formation, which was further supported by experimental results of the visible-light-induced water oxidation reaction. This work highlighted for the first time the application of a SPR photocatalyst for a two-step photoexcitation system through combination with WO₃. It represents the successful attempt to use both SPR and band-gap excitation for photochemical reactions.¹⁴⁴



3.2.3 Photocatalytic CO₂ conversion to hydrocarbon fuels.

Besides the photocatalytic or photoelectrochemical water-splitting reactions, AuNP-based plasmonic photocatalysts have

also been used to catalyze other energy-conversion reactions, especially photocatalytic methane formation upon reduction of CO₂ by H₂O:



For example, Hou *et al.* reported the use of the Au/TiO₂ plasmonic photocatalyst to convert CO₂ to hydrocarbon fuels.¹⁴⁵ Under visible illumination ($\lambda = 532\text{ nm}$), a 24-fold enhancement in the photocatalytic activity was highlighted due to the intense local electromagnetic fields created by the surface plasmons of the AuNPs (Fig. 16a). Various reduction products such as CH₄, HCHO, and CH₃OH are detected because of the differences in the conduction and valence band energies of TiO₂ with the reduction potentials of CO₂ (Fig. 16b). More recently, Zhang *et al.* fabricated TiO₂ nanofibers that were codecorated with AuNPs and PtNPs (Au/Pt/TiO₂NFs) and used these photocatalysts to evaluate the activities in hydrogen production.¹⁴⁶ These studies suggested that PtNPs mainly contributed to the active sites for H₂ production. The photoreduction of CO₂ by water vapor was also employed to confirm the contribution of codecorated AuNPs to the photocatalytic activity, which showed that the synergy of the electron-sink function of Pt and SPR of AuNPs significantly improved the charge separation of photoexcited TiO₂ and resulted in great enhancement in photocatalytic activities for both H₂ generation and CO₂ reduction. This catalyst design provided a more effective way to harvest solar energy for fuel production, which could inspire future work in this area.

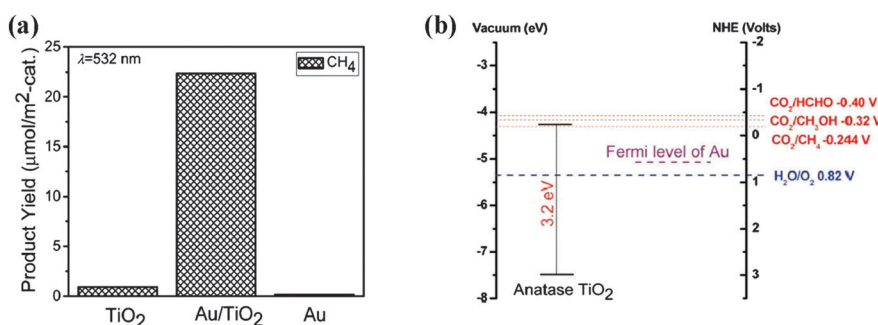


Fig. 16 (a) Photocatalytic product yields (after 15 h of visible irradiation) on three different catalytic surfaces. (b) Energy band alignment of anatase TiO₂, Au, and the relevant redox potentials of CO₂ and H₂O under visible illumination. Reprinted with permission from ref. 145. Copyright 2011, American Chemical Society.

4 Mechanistic overview

From the examples discussed in Section 3, the photocatalytic properties of AuNP-based plasmonic photocatalysis were often described as greatly enhancing the photocatalytic activity or high conversion with high selectivity to the target product. The question is raised, however, concerning what is responsible for those superior photocatalytic functions. In order to illustrate the potential mechanism of LSPR-enhanced photocatalytic properties under visible light illumination, two mechanisms have been widely used: the charge-transfer mechanism and the local-electric-field enhancement mechanism. These two possible mechanisms and other possible mechanisms are now discussed in some detail.

4.1 Charge-transfer mechanism

The charge-transfer mechanism was proposed by Tian *et al.* when they reported visible-light irradiation ($\lambda > 420$ nm) of AuNPs on a semiconductor TiO₂ film coated on an indium-tin-oxide electrode. This system generated an anodic photocurrent in the presence of Fe²⁺. The charge-transfer mechanism was proposed by these authors to explain the experimental observation of photo-to-current conversion efficiency enhancement.⁵² Generally, this mechanism is depicted as follows: when the plasmonic AuNPs are irradiated with visible light, the collective oscillation of electrons on the AuNPs excited by the LSPR is induced by the incident visible light, and conduction electrons (e⁻) are transferred from AuNPs to the conduction band of the semiconductor, while the positively charged AuNPs receive e⁻ from electron donors such as Fe²⁺, HCHO and alcohol molecules.¹⁵

The charge-transfer mechanism was found to be more functional in the composite photocatalyst structures, in which the direct contact between plasmonic metal NPs and semiconductor allows the rapid charge-carrier transfer.¹¹ For example, as shown in Fig. 17a, in the aerobic oxidation of alcohol reactions, this oxidation reaction and reduction of O₂ by e⁻ (formation of O–O⁻ species) occur simultaneously over AuNPs and the conduction band of TiO₂, respectively. Then, the O–O⁻ species attracts the H atom of the alcohol and produces Au-alcoholate species. Subsequently, H atoms from Au-alcoholate

species are removed to produce the carbonyl products. This e⁻ transfer from photoactivated AuNPs to TiO₂ and subsequent O₂ reduction on the TiO₂ surface was confirmed by ESR analysis.⁸⁶ However, in the water-splitting reactions, the mechanism is more complicated. Due to the alignment of the electronic states, plasmonic metal NPs/semiconductor composite photocatalysts only allow for the transfer of energetic electrons from the metal NPs to the semiconductor. All the plasmonic charges residing at the Fermi energy of the metal cannot drive the reduction and oxidation half-reactions, because the plasmonic electrons (at E_F) are too low in energy to drive the reduction half-reaction, and the plasmonic holes (also at E_F) are too high in energy to drive the oxidation half-reaction.¹⁴⁷ Therefore, in order to successfully take into account the excitation of the electrons by the LSPR and their transfer from metal NPs to the semiconductor, the working mechanism must involve three continuous steps (Fig. 17b): (i) the electrons on the plasmonic metal near the metal Fermi level are excited to the surface plasmon (SP) states under the visible light irradiation; (ii) the excited electrons then transfer to the adjacent semiconductor; (iii) the electron transfer in steps (i) and (ii) activates the electron-driven processes in the O₂ evolution half-reaction ($\text{H}_2\text{O} + 2\text{h}^+ \rightarrow 1/2\text{O}_2 + 2\text{H}^+$) and H₂ evolution half-reaction ($2\text{H}^+ + 2\text{e}^- \rightarrow \text{H}_2$).¹¹ Moreover, in photoelectrochemical water splitting, plasmonic Au nanocrystals coupled to TiO₂ nanotubes with top seamless photonic crystal layer (AuNCs/TiO₂ NTPC) showed excellent PEC water-splitting performances due to the SPR-induced electron transfer, which inspired the design of plasmonic-photonic crystal systems to prepare efficient visible-light photocatalysts.¹⁴⁸

In Au/TiO₂ catalytic systems promoted by the charge-transfer mechanism, the location of AuNPs was found to be crucial for the promotion of electron transfer from LSPR excited AuNPs to various kinds of TiO₂. As mentioned previously, AuNPs with < 5 nm diameter located at the interface of anatase/rutile TiO₂ particles behave as the active sites for the photoreaction. Plasmon activation of the AuNPs consecutively transfers conduction electrons from AuNPs to rutile and then to adjacent anatase TiO₂, thus catalyzing the oxidation of organic substrates⁸⁶ and decomposition of MB at room temperature.¹²² Very recently,

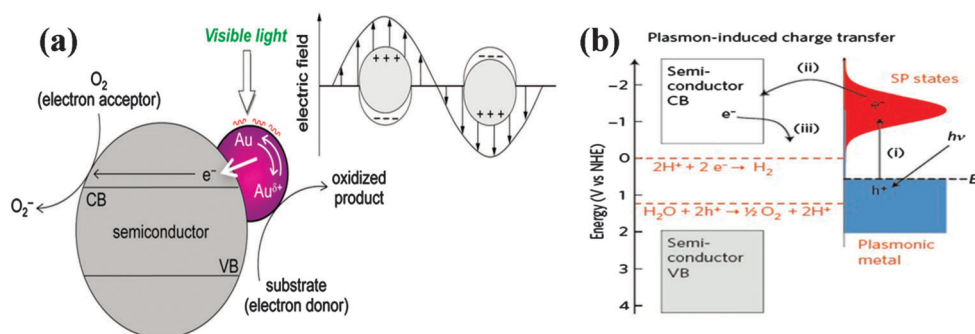


Fig. 17 LSPR induced charge-transfer mechanism: (a) aerobic oxidation by AuNPs/semiconductor, (b) water splitting with approximate energy levels on the NHE scale by the plasmonic metal/semiconductor. Reprinted with permission from ref. 11 and 86, Copyright 2012 American Chemical Society and 2011 Nature Publishing Group, respectively.

AuNPs located on the basal surface of the anatase TiO_2 mesocrystal were found to be much more effective in transferring electrons from the LSPR excited AuNPs to the MesoTiO_2 system than those located on the lateral surfaces of MesoTiO_2 prepared by a PD method. In order to provide evidence of this ultrafast electron-transfer process, time-resolved diffuse reflectance spectroscopy was used to measure the lifetime of the injected electrons. This suggested that electron accumulation time in the Au/MesoTiO_2 system (5.6 min) is significantly shorter than those in the $\text{Au/MesoTiO}_2\text{-PD}$ (16 min) and Au/TiO_2 NP systems (10–26 min). Indeed, >60% electrons in the Au/MesoTiO_2 system have a prolonged electron lifetime of ~ 10 ns in ambient air, while the electrons in the $\text{Au/MesoTiO}_2\text{-PD}$ and Au/P25 TiO_2 systems recombine with the holes in the Au NPs within a few nanoseconds.¹¹⁸ Thus, the importance of the location of AuNPs on semiconductors is that it may significantly retard the charge recombination process of the electrons, thereby enhancing the visible-light photocatalytic performance.

4.2 Local electric field enhancement mechanism

As mentioned above, plasmonic metal NPs have their own absorbance spectral surface plasmon band. When plasmonic metal NPs are irradiated with visible light with the wavelength near their plasmon resonance frequency, the incoming photons are absorbed, and the optical absorption produces a local electric field near the surface of the NPs. Excited plasmonic NPs act as concentrators and the LSPR greatly enhances the intensity of electric field. Then, the enhanced local field would in turn boost the generation rate of electron-hole pairs in semiconductors by a linear or nonlinear relationship. Thus, the probability of a photocatalytic reaction is high compared to that of $\text{e}^- - \text{h}^+$ recombination.¹¹

The estimation of the induced electromagnetic field enhancement is mainly based on Maxwell's classic electromagnetism theory (the finite-difference time-domain (FDTD) method). Electromagnetic simulations using the FDTD method have shown that the induced electromagnetic field enhancement is approximately 10–100 times larger than the incident electromagnetic field intensity. Surprisingly, in the “hot spot” regions, the electric-field intensity of local plasmonic “hot spots” can reach as much as 1000 times that of the incident electric field.^{65,149} For example, Cronin's group performed FDTD numerical simulations of electromagnetic response to study the enhanced electric-field intensities at the interface of Au-TiO_2 .^{112,128} The enhanced electric fields are observed local “hot spots” that can be clearly seen in regions between nearly touching AuNPs (Fig. 18a and b). Furthermore, a cross-sectional plot of the electric fields in one of these hot-spot regions illustrates that the electric-field intensity at the TiO_2 surface reaches 1000 times that of the incident electric field (Fig. 18c). This greatly enhances the rate of $\text{e}^- - \text{h}^+$ pair formation in the near-surface region, thereby leading to the overall enhancement in the photocatalytic water-splitting activity by factors of 5 and 66 at wavelengths of 532 nm and 633 nm,¹²⁸ respectively, and 9-fold improvement in the photocatalytic decomposition rate of methyl orange.¹¹²

An enhancement in the local electric field benefits from the successful design of the photocatalyst structure due to the enhancement in the local electric field that was found to be highly dependent on the size¹⁴² and shape of the plasmonic metallic NPs.¹⁵⁰ Recently, Wang *et al.* prepared $\text{Au/TiO}_2/\text{Au}$ plasmonic coupling photocatalysts by first growing TiO_2 nanosheets directly on a Ti foil, then depositing AuNPs on both sides of these nanosheets. More importantly, the maximum electric-field

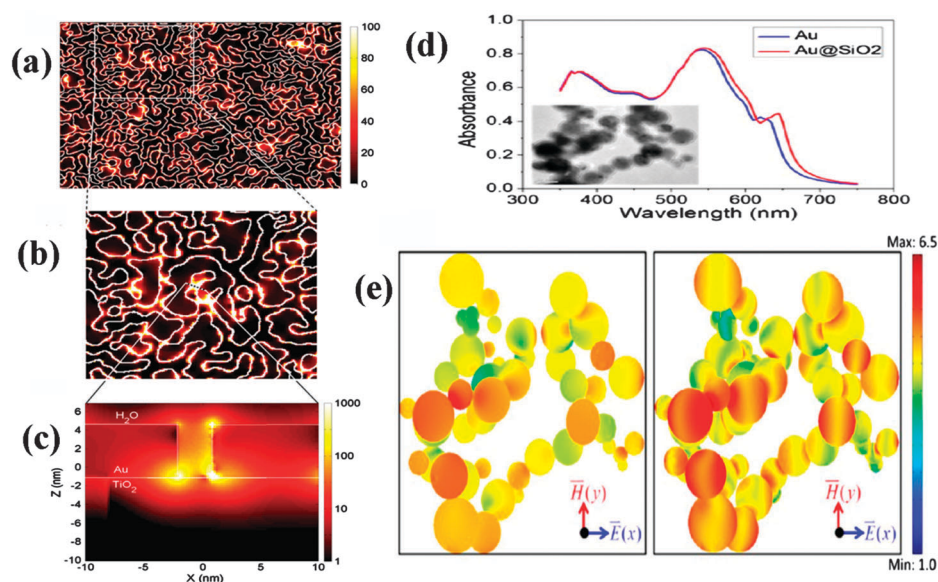


Fig. 18 (a–c) Electric-field intensity at the interface of Au-TiO_2 calculated using FDTD. (d) Simulated spectra for x -polarized illumination of AuNPs only (blue line) and AuNPs covered with 3 nm SiO_2 (red line) in water. The inset shows the TEM image of SiO_2 -covered AuNPs. (e) Simulated electric-field intensity on the outer surface of AuNPs (left) and Au-SiO_2 core-shell NPs (right) at plasmonic wavelength on the logarithmic scale. The wavelength of incident light is 540 nm (left) and 545 nm (right). Reprinted with permission from ref. 112 and 120. Copyright 2011 Elsevier and 2012 American Chemical Society, respectively.

intensity enhancement of the Au/TiO₂/Au nanostructure is 38-fold through the calculation of the FDTD method.¹⁵¹ The electric-field intensity can be enhanced in both cases of Au and Au@SiO₂ core-shell nanoparticles by their LSPR (Fig. 18d). But, as shown in Fig. 18e, the electric-field intensity on the outer surface of Au@SiO₂ core-shell nanoparticles is 8.98 times higher than that of bare AuNPs. When Au@SiO₂ and AuNPs were separately deposited on TiO₂, the enhancement of the local electric field of the former was also observed to be larger than that of the latter, which can be attributed to the promoted LSPR that can assist in generating more e⁻-h⁺ pairs inside the TiO₂ thin film to compensate the loss of the electron trap effect due to SiO₂ insulation.¹²⁰ However, a Janus Au-TiO₂ nanostructure was more efficient than its core-shell counterpart due to strong, non-centrosymmetric localization of the plasmonic near-fields on one side of the AuNPs in Janus Au-TiO₂ nanostructures that was different from the symmetric near-field enhancement of the electric field in Au-TiO₂ core-shell nanostructures.¹⁴² More importantly, the photodegradation of MB rate of Au/Ag/TiO₂ ($1.06 \times 10^{-2} \text{ min}^{-1}$) was much higher than that of Au/TiO₂ ($3.73 \times 10^{-3} \text{ min}^{-1}$) under irradiation with visible light (500–700 nm), because the AgNRs displayed higher electric-field enhancements than AuNRs, and the Fermi level of Au/Ag NRs became closer to that of TiO₂ upon Ag coating.¹⁵²

Additionally, in core-shell or sandwich nanostructured plasmonic photocatalysis, the distance between the plasmonic metal NPs and the semiconductors also plays a role in determining the enhancement factor in the near field. Torimoto *et al.* indicated that the photocatalytic activity of Au@SiO₂/CdS for H₂ evolution was greatly dependent on the distance between CdS and AuNPs, due to the locally enhanced electric field produced by photoexcitation of the LSPR of AuNPs.¹⁴³ Plasmonic coupling in various metallic layers plays a determining role in the LSPR properties. Very recently, the LSPR properties of Au-Ag-Au three-layered nanoshells were investigated theoretically using quasi-static electricity by Zhu *et al.* Thus multilayered nanoshells constituted with various metals alternately appearing created abundant LSPR modes and were easily tuned by altering the geometric factors of different metallic layers.¹⁵³ All these examples gave further support of the local electric-field-enhancement mechanism.

4.3 Mechanism in large NPs

Apart from these two main mechanisms, another mechanism that was usually used is the scattering mechanism normally occurring for large plasmonic nanostructures (larger than ~50 nm in diameter). Generally, the resonant photons that are not absorbed by a semiconductor are scattered by larger plasmonic metal NPs, ultimately increasing the average path length in plasmonic nanostructures and the rate of e⁻-h⁺ pair formation in the semiconductor. The efficiency of scattering is sensitive to the size, shape and the loading level of the plasmonic metal NPs. For example, high loading of plasmonic metal NPs leads to the absorption of many photons in the first interaction with metal NPs, leaving only a few for multiple scattering, while the influence of scattering is negligible with low plasmonic metal

NP loading.²⁸ The scattering mechanism is widely used to illustrate the working mechanism for the LSPR-enhanced photoactivity in Ag based plasmonic photocatalysis.^{11,132,154,155} However, for AuNP-based plasmonic photocatalysts, this mechanism has rarely been examined.

5 Conclusions and outlook

In summary, the introduction of SPR/LSPR into photocatalysis under visible-light irradiation can efficiently improve the photocatalytic activity and modify the product selectivity. Using plasmonic photocatalysts to catalyze chemical reactions is promising, and the obtained results are encouraging. The knowledge of the traditional photocatalysts has been recently updated by recognizing that the LSPR effect of noble-metal NPs can significantly improve the photocatalytic ability of their adjacent semiconductors, resulting in better photocatalytic functions. However, the use of plasmonic photocatalysts to catalyze chemical reactions is a new field, and its applications are challenging. From our perspective, several challenges need to be overcome as illustrated below:

First, the physical understanding of plasmonic photocatalysis requires more studies, especially the unified and widely-accepted predictive models to guide the effective design of stable, low-cost and efficient AuNP-based plasmonic photocatalysts.

Secondly, though some efforts have been made to illustrate the working mechanism of plasmonic photocatalysts, the electron-transfer pathway is not fully understood. For example, the determination of the electron-transfer process from plasmonic AuNP to its adjacent semiconductor or to the absorbed molecules is crucial to the associated photocatalytic properties. In addition, AuNP size, shape and other parameters are sensitive to the LSPR absorption, which may affect the electron-transfer efficiency and the final photocatalytic performance.

Thirdly, although the use of Au-based plasmonic photocatalysis has been extended to various reactions, the reaction types are still limited. The applications could be extended to various practical reactions, for which fundamental work is needed to control the photocatalytic functions in various experimental systems.

Fourth, the reported studies currently used relatively large AuNPs, making the nominal turnover number (TON) in relation to Au atoms very small.² Moreover, the available publications mainly focused on the near UV and visible light, and only a few works concentrated on extending the wavelength response region to near infrared using plasmonic photocatalysis.²⁸

It is reasonable to believe that with significant attention paid to this area, the challenges mentioned above will be worked out in the forthcoming years. Since the physical, technological and experimental breakthroughs are forthcoming, widespread applications of AuNP-based plasmonic photocatalysts should make it possible to disclose greener, safer and more effective processes for chemical reactions.

Finally, all the selected examples of Au-based plasmonic photocatalysts discussed in Section 3, including the type of catalysts, main size, structure, the catalyzed reaction, light resource,

Table 2 Examples of Au-based plasmonic photocatalysts that are discussed in Section 3

Catalysts	Preparation method	Au size (nm)	Structure	Photocatalytic reactions	Light source	Main photocatalytic performance	Ref.
Au/CeO ₂	Photodeposition	$d_{\text{Au}}: 59 \pm 4.9$ (SS), 92 ± 8.0 (MS)	Nanoparticles	Oxidation of aromatic alcohols	Green light-emitting diode	Conv. (%) sel. (%) SS: 14–45, > 99 MS: 17–59, > 99	24
Au/TiO ₂	<i>In situ</i> , photo-deposition and SMAD	$d_{\text{Au}}: 8\text{--}70$	Nanocomposites	Water splitting	50 W high pressure Hg lamp <i>via</i> a quartz tube	H ₂ evolution rate <i>In situ</i> : 1200 $\mu\text{mol h}^{-1}$ Photodeposition: 920 $\mu\text{mol h}^{-1}$ SMAD: 1600 $\mu\text{mol h}^{-1}$	25
Au–Pd@ZrO ₂	Impregnation–reduction	NP size < 8 nm	Binary alloyed NPs	Miyaura–Suzuki coupling reaction, oxidative addition of benzylamine, selective oxidation of aromatic alcohols and phenol oxidation	500 W halogen lamp ($\lambda = 400\text{--}750$ nm)	Au/Pd ratio of 1:1.86 showed best photocatalytic activity	83
Au–Pd@ZrO ₂	Impregnation–reduction	NP size < 10 nm	Binary alloyed NPs	Dehydrogenation of aromatic alcohols	500 W halogen lamp ($\lambda = 400\text{--}750$ nm) and 50 W high power LED lamps	Au/Pd ratio of 1:1.86 showed best photocatalytic activity	84
Au/P2.5 TiO ₂	Deposition–precipitation	$d_{\text{Au}} < 5$ nm	Nanoparticles	Aerobic oxidation of alcohols	Xe lamp ($\lambda > 450$ nm, white bars) and sunlight	Sunlight: conv. (%): 79–> 99, sel. (%): 79–99	86
Au@Pd/TiO ₂	Two-step photodeposition	$d_{\text{Au}}: 9.6$ nm	Core–shell	Photocatalytic dechlorination of chlorobenzene to benzene along with oxidation of 2-propanol to acetone	500 W Xe lamp filtered with a Y-48 cut filter (450–600 nm: 83 mW cm ^{−2})	20 h: benzene selectivity: > 99%, chlorobenzene conversion: 99%	88
Au@TiO ₂	<i>In situ</i>	$d_{\text{Au}}: 20\text{--}80$ nm	Nanocomposites	Oxidation of benzene to phenol	300 W Xe arc lamp ($\lambda > 400$ nm)	63% yield and 91% selectivity	53
Au/TiO ₂	Photodeposition	Au(0.25 × 4)/TiO ₂ (723) size: smaller (1.4 nm) and larger (13 nm)	Nanoparticles	H ₂ formation from 2-propanol and ammonia, and mineralization of acetic acid	500 W Xe lamp filtered with a Y-48 filter (450–600 nm: 83 mW cm ^{−2})	In the case of H ₂ formation under deaerated conditions, the reaction rate of Au/TiO ₂ having both larger and smaller particles was 4-times larger than that of the Au/TiO ₂ sample without smaller AuNPs	89
SiO ₂ /Au/TiO ₂	Sol–gel and calcination processes	$d_{\text{Au}}: 8\text{--}15$ nm	Sandwich	Degradation of organic molecules	UV, visible light, and sunlight	Sunlight: degradation > 93% within 40 min	90
Au@Cu ₂ O Au@SiO ₂ Au@SiO ₂ @Cu ₂ O AuNP	Encapsulation Photochemical	$d_{\text{Au}}: 20$ nm $d_{\text{Au}}: 15$ nm	Core–shell sandwich Nanosphere	Degradation of methyl orange Oxidation of <i>sec</i> -phenethyl and benzyl alcohols	Visible light lamps ($\lambda = 400\text{--}700$ nm) and Xe lamp 532 nm laser drop irradiation, 530 nm LED and microwave irradiation 530 nm LED	Au@SiO ₂ @Cu ₂ O exhibited the best photocatalytic activity 95% <i>sec</i> -phenethyl alcohol conversion in 20 min under 530 nm LEDs irradiation	91 93
Au/HT Au/ <i>r</i> -Al ₂ O ₃ Au/ZnO Au/ <i>n</i> -Al ₂ O ₃ AuPd	Dry/ablation photochemical Wet-chemical reduction	Au/HT $d_{\text{Au}}: 21 \pm 10$ (dry) $d_{\text{Au}}: 9 \pm 3$ nm (ablation) Average edge length and thickness were 290 and 6 nm, respectively	Nanocomposites Nanowheels	Oxidation of <i>sec</i> -phenethyl and benzyl alcohols Benzyl alcohol oxidation and Miyaura–Suzuki coupling reaction	530 nm LED	Au/HT: yielding 90% acetophenone after 40 min of LED irradiation	94
Au/CeO ₂	Photodeposition	$d_{\text{Au}}: 59.3$ nm	Nanocomposites	Oxidation of benzyl alcohols	Xe lamp Green light from LED	6 h benzyl alcohol oxidation: conversion: 97.7%, Benzaldehyde selectivity: 98.0%. Suzuki reaction: 3.8 times greater than conventional heating conditions (conversion at 60 min) 20 h photoirradiation: no CO ₂ was detected Benzaldehyde selectivity: > 99%, benzyl alcohol conversion > 99%, carbon balance: > 99%	95 96

Table 2 (continued)

Catalysts	Preparation method	Au size (nm)	Structure	Photocatalytic reactions	Light source	Main photocatalytic performance	Ref.
Au-Cu/TiO ₂	Deposition-reduction	$d_{\text{NP}}: 3.4 \pm 0.8$ nm	Spherical alloy NPs	Aerobic oxidation of alcohols	2 kW Xe lamp ($\lambda > 450$ nm) and sunlight	Sunlight: conv. (%): 72–88 Sel. (%): 71–88	97
Au/zeolite	Impregnation-reduction	Au/A (8.3 nm), Au/beta (12.9 nm), Au/Y (8.1 nm), Au/silicalite-1 (13.2 nm), Au/TS-1 (8.2 nm) and Au/ZSM-5 (9.1 nm)	Nanoparticles	Oxidation of aromatic alcohols to aldehydes	500 W halogen lamp (0.42 W cm ⁻² ; 400–800 nm)	Photooxidation of benzyl alcohol conversion at 25 °C on the Au/Y catalyst was 27.1% (1.0% in the dark). The selectivity to aldehyde is 99%	98
Au/SiO ₂		Au size: 1.85 ± 0.55 nm	Spherical AuNPs	Amidation reaction	A solid state 532 nm green laser	3 h of reaction: alpha-methyl benzylamine (99% conversion, 98% selectivity to the corresponding amide) 5 h of reaction: benzylamine (97% conv., 95% sel. to N-benzylbenzamide) AuNR/TiO ₂ -660 and AuNR/TiO ₂ -710 observed 9 and 2 times, respectively, as many as that obtained under dark reaction	99
Au/TiO ₂	Seed-mediated synthetic route + incipient wetness impregnation method	AuNRs longitudinal length (ca. 40 nm) with different aspect ratios (ca. 1.8, 2.3, 2.7, 3.3, 4.0)	Gold nanorods	Photocatalytic oxidation of 2-propanol	300 W Xe lamp		100
Au/TiO ₂ -Ag	Photodeposition with CPH method	Au size: 13 ± 1.4 nm	Au nanoparticles	Photocatalytic reduction of nitrobenzene in a 2-propanol suspension	500 W Xe lamp filtered with a Y-48 cut filter (450–600 nm: 83 mW cm ⁻²)	10 h: aniline sele. > 99%, nitrobenzene conv. > 99%	101
Au/TiO ₂ -M	Photodeposition and CPH method	Au size: 13 nm	Au nanoparticles	Formation of H ₂ and acetone from 2-propanol	500 W Xe lamp ($\lambda = 450$ –600 nm)	H ₂ formation rates of Au/TiO ₂ -M depended on M and decreased in the order of M: Pt > Pd > Ru > Rh > Au > Ag > Cu > Ir Au/Ag = 1 : 5 and TiO ₂ shell thickness of 10 nm showed the best activity	102
Au/Ag/TiO ₂	Encapsulation	Au nanorods: longer axis: 44.2 nm and the shorter axis: 10.4 (aspect ratio is 4.3)	Trilayered nanorod	Oxidation of 2-propanol	200 W Xe lamp ($\lambda > 420$ nm) equipped with a UV cut filter (Kenko U-420)		103
Ag/TiO ₂ Au/TiO ₂	Depositing and annealing	Au size: 20–30 nm	Quasi-spherical AuNPs and AgNPs	Photooxidation of methanol and ethylene	Hg and Xe arc lamp systems and the UV-LED	Catalysts show enhanced activity (up to ×100 for some configurations) compared to bare TiO ₂	104
Au/ZrO ₂	Impregnation-reduction	Au size: 6 nm	Nanoparticles	Reduction of nitrobenzene	Incandescent light or UV light	3 wt% Au/ZrO ₂ : 100% nitrobenzene was reduced and azobenzene was more than 99% (after 5 h)	105
Au/CeO ₂	Impregnation-reduction	Au-NPs were estimated to be 2 nm, 5 nm and 8 nm	Nanoparticles	Photocatalytic reductions	An incandescent light	5 nm Au/CeO ₂ exhibits the highest photocatalytic activity in reducing styrene oxide	106
Au/CeO ₂ Au/TiO ₂ Au/ZrO ₂ Au/Al ₂ O ₃ Au/zeolite Y	Impregnation-reduction	Au size: 5–8 nm (Au/CeO ₂ , Au/TiO ₂ and Au/ZrO ₂), 3 nm (Au/Al ₂ O ₃) and 10 nm (Au/zeolite Y)	Nanoparticles	Photocatalytic reduction	Halogen lamp and incandescent light	Au/CeO ₂ exhibited the high catalytic activity	107
Au/MOs (metal oxides)	Heating temperature-varied deposition	$d_{\text{Au}} = 6.7$ nm (Au/rutile TiO ₂)	Nanoparticles	One-step selective aerobic oxidation of amines to imines	300 W Xe lamp with a cut off filter Y-45	Au/rutile TiO ₂ in amines yields the corresponding imines on a synthetic scale with high selectivity (> 99%) under solvent-free conditions at 298 K	108
Au/TiO ₂ -N	precipitation Impregnation-reduction	$d_{\text{Au}}: 4.6$ –5.1 nm	Nanoparticles	Hydroamination of alkynes	500 W halogen lamp and LEDs	The highest conversion: 90% for 4-phenyl-1-butene with a selectivity of 91% to imine	109

Table 2 (continued)

Catalysts	Preparation method	Au size (nm)	Structure	Photocatalytic reactions	Light source	Main photocatalytic performance	Ref.
Au@ZnO	Commercial		Nanoparticles	Propargylamine synthesis	LED irradiation ($\lambda > 450$ nm)	Propargylamines with good yields (50–95%) at room temperature	110
Au@P25	Deposition–reduction	Au size: 5–10 nm	Nanoparticles	Selective photocatalytic benzene oxidation	Solar simulator	13% yield and 89% selectivity of phenol was obtained on Au@P25 under 230 kPa of CO ₂	111
Au/TiO ₂	Depositing	AuNP film with a nominal thickness of 5 nm	Au island film	Photocatalytic decomposition of MO	UV Hg lamp or green laser irradiation	9-fold improvement in the photocatalytic decomposition rate of methyl orange driven by Au/TiO ₂	112
Au@TiO ₂	Wet chemical bottom-up deposition	36 ± 6 nm	2D array AuNPs	Photodegradation of methylene blue	300 W Xe lamp equipped with Vis (385–740 nm)	Highest photocatalytic activity with visible irradiation was 1.7 times higher than that of TiO ₂ with UV irradiation	113
Au–TiO ₂	Silica template method and chemical etching treatment	d_{Au} : ~10 nm	AuNP + TiO ₂ nanocups/hollow spheres	Photodegradation of methylene blue	Visible light source (780 nm $\geq \lambda \geq 400$ nm)	Photodegradation rate constants over Au–P25, Au–TiO ₂ HSS, and Au–TiO ₂ nanocups are 0.516×10^{-2} , 1.506×10^{-2} , and $2.211 \times 10^{-2} \text{ min}^{-1}$, respectively	114
Au _x /TiO ₂ -001 (Au wt% = 0.5, 1.0 and 2.0)	Sulfide-mediated polyol process with modifications	d_{Au} : ca. 5 nm	Nanoparticles	Photocatalytic degradation of RhB	300 W Xe lamp with a 420 nm cut-off filter	Photocatalytic reaction rate constants: Au _{1.0} /TiO ₂ -001 > Au _{0.5} /TiO ₂ -001 > Au _{2.0} /TiO ₂ -001 > N/TiO ₂ > TiO ₂ -001	115
Au nanocrystal/titanate nanobelt heterojunctions	Brust method + self-assembly	Homogeneous structures: width of 70–80 nm and the length of several micrometers	Au nanocrystals	Degradation of MO	UV and visible light illumination from the light source of 125 W high-pressure Hg lamps	Photo-degradation rate was 99.8% and 99.5% over 5 wt%-Au/titanate under 120 min UV-light and 300 min visible light irradiation, respectively	116
Au/TiO ₂	Green synthetic method	Au size: 8–20 nm	Nanoparticles	Degradation of MO dye	Sunlight	2 wt% gold (2Au/TiO ₂ -9-2) exhibits 2.5 times higher degradation activity towards methyl orange dye compared to Degussa P-25 TiO ₂ under solar light irradiation	117
Au/MesoTiO ₂	Impregnation method; photochemical deposition method	Au size: 30–80 nm	AuNPs + anatase TiO ₂ mesocrystal superstructures	MB, RhB and 4-CP photodegradation; H ₂ production from 2-propanol–water	Xe light source through the filters (460 nm < λ < 700 nm)	Au/MesoTiO ₂ yield more than 1 order of magnitude of enhancement in the visible-light photocatalytic activity	118
SiO ₂ @TiO ₂ -Au		Au size: 5, 15 and 30 nm	Core@shell	MB, MO and PNP photodegradation	450 W Xe lamp equipped with a 420 nm cutoff filter	Au NP arrays with 15 nm size and 700 μm^{-2} density showed maximum catalytic efficiency	119
Au@SiO ₂ /TiO ₂	Thermal hydrolysis + sodium citrate reduced method	Average Au core diameter of 50 nm and silica shell thickness of nearly 3 nm	Core@shell structure (shell-isolated)	Photocatalytic degradation of MB	UV (365 nm) and the Xe lamp with filter (400 nm < λ < 700 nm)	MB degradation efficiency of 95% under UV + visible light irradiation in 5 h	120
Au/KNbO ₃	Deposition–precipitation	Au size: 5.8–10.8 nm	Nanocomposites	Degradation of RhB	300 W Xe lamp ($\lambda > 420$ nm; 180 mW cm^{-2}) and a UV bandpass filter (365 ± 12 nm; ca. 150 mW cm^{-2})	The reaction rate constant of Au/KNbO ₃ NWs (Au NP size of 10.8 nm) under UV is about 4 times than that under visible-light, and exceeds that of commercial KNbO ₃ by a factor of 15	121
Au _x (DP _y)/TiO ₂	Deposition–precipitation	d_{Au} in Au ₃ (DP ₃₅₀)/TiO ₂ was 4.16 nm	Nanoparticles	Decomposition of MB	350 W Xe lamp with a cutoff filter of 420 nm	The optimal photocatalytic activity was obtained in Au ₃ (DP ₃₅₀)/TiO ₂	122
Au@ZnO	New colloidal method	Au size: 75–100 nm	Core–shell	Degradation of MO	150 W Xe lamp with a 390 nm cut-off filter	Significant enhancement at the wavelengths corresponding to LSPR of Au core	123
Au/TiO ₂	Deposition–precipitation	d_{Au} = 2.1 nm	Nanoparticles	Degradation of nonylphenol	300 W Xe lamp with a cut off filter Y-45	Au/rutile TiO ₂ exhibits much higher visible-light activity than Au/anatase TiO ₂ and BiVO ₄	124

Table 2 (continued)

Catalysts	Preparation method	Au size (nm)	Structure	Photocatalytic reactions	Light source	Main photocatalytic performance	Ref.
Au/TiO ₂	Colloid impregnation (CI), colloid salting-out (CS), colloid photodeposition (CP), and colloid photodeposition with a hole scavenger (CPH)	Colloidal Au nanoparticles, revealing that AuNP size: 12.8 ± 1.4 nm	Nanoparticles	Mineralization of oxalic acid and acetic acid in aqueous suspensions	Xe lamp with an O-54 cutoff filter and IR cutoff filter	Very large reaction rates were obtained in the samples with 5 wt% Au or more	125
SiO ₂ -Au	Seed growth + depositing	Diameter of 5 ± 1.6 nm	Au nanospheres	Decompose methyl orange and trichloroethylene	532 nm green laser at different intensities (0.2 W, 1 W and 2 W)	Reaction rate for green laser irradiation at 0.2 W, 1 W and 2 W are 0.001 min ⁻¹ , 0.0028 min ⁻¹ and 0.0163 min ⁻¹	126
Au-Pd	Two-step seeded-growth	Average diameters/lengths of the medium and small nanostructures are 30 ± 3/61 ± 6 and 30 ± 3/53 ± 5, respectively	Au nanorods	Suzuki coupling reactions	A continuous semiconductor laser diode at 809 nm and solar radiation	14 reactions under solar radiation: yields: 50–99%, with nine of them were above 96%	127
Au/TiO ₂	Electron beam evaporation	Gold film with a nominal thickness of 5 nm	Island-like	Photocatalytic splitting of water	UV irradiation and visible irradiation ($\lambda = 532/633$ nm, 0.15 W cm ⁻²)	Enhancement factors in the photocatalytic activity were of 5 and 66 at wavelengths of 532 nm and 633 nm, respectively	128
Au/TiO ₂	Photodeposition	AuNP size: 20 nm	Near spherical Au particles	Degradation of methyl orange; H ₂ evolution in photocatalytic water splitting	Xe lamp ($\lambda > 400$ nm)	The extra ~13% increase in MB degradation was attributed to the SPR on AuNPs; additional visible light further boosted the H ₂ yield of Au/TiO ₂ to 53.75 $\mu\text{mol g}_{\text{cat}}^{-1}$	130
Ag/N-TiO ₂ Au/N-TiO ₂		Ag nanocubes: edge length of 118 ± 25 nm; Au size: 24.5 ± 4.5 nm	Ag nanocubes Au spheres	Photoelectrochemical water splitting	Broadband visible source (400–900 nm, ~500 mW cm ⁻² , spectral peak at 580 nm)	AgNPs to N-TiO ₂ increases the visible-light photocurrent by a factor of ~10. AuNPs have only a small effect on the photocurrent	57
AuNR/NP-TiO ₂	Seed-growth process + immersing	The length and width of AuNRs were 40 and 15 nm, respectively	Au nanorod Au nanoparticles	Photoelectrochemical water oxidation	Visible-light illumination by adding a 430 nm long-pass filter to the white light source regions	As compared with bare TiO ₂ , AuNP-TiO ₂ electrodes exhibited significantly enhanced photoactivity in both the UV and visible regions	132
Au/TiO ₂ -Pt	Photodeposition	Au size: 13 ± 1.4 nm	Au nanoparticles	Water oxidation and Cr(vi) reduction	Green light emitting diode	For AuNR/NP-TiO ₂ , the photoactivity enhancement was only observed in the visible region	133
Au-TiO ₂	Co-polymer assisted sol-gel method	Au size: 12.9 nm	Nanocomposites	H ₂ evolution from photocatalytic water reduction	300 W Xe lamp coupling with a UV cutoff filter ($\lambda > 420$ nm)	AuNR/NP-TiO ₂ showed enhanced photoactivity in the entire UV-visible region	134
Au-TiO ₂	Deposition-precipitation	Au size: 5 nm	3D Au-TiO ₂ aerogels	Photoelectrochemical water splitting	500 W Xe arc lamp fitted with a monochromator	Au/TiO ₂ -Pt exhibited a reaction rate about twice larger than that of Pt-free Au/TiO ₂	135
Au/ZnFe ₂ O ₄ /ZnO	Pulsed laser deposition (PLD) + DC magnetron sputtering	Au size: 8–10 nm	Au nanoparticles	Photoelectrochemical water splitting	1 sun (AM 1.5 conditions, Newport solar simulator)	2% Au-TiO ₂ shows the highest photocatalytic activity	136

Table 2 (continued)

Catalysts	Preparation method	Au size (nm)	Structure	Photocatalytic reactions	Light source	Main photocatalytic performance	Ref.
Au-TiO ₂	Multi-step and single-step photodeposition method	Average diameter of AuNP: SS-(1.00)Au/TiO ₂ : 1.2 nm; MS-(1.00)Au/TiO ₂ : 1.3 nm	Au nanoparticles	H ₂ production from 2-propanol, ethanol, methanol, ammonia and benzyl alcohol	500 W Xe lamp filtered with a Y-48 filter (450–600 nm: 83 mW cm ⁻²)	MS-(1.00)Au/TiO ₂ shows higher levels of activity for H ₂ production	137
Au/TiO ₂	Deposition-precipitation	AuNP average size: 5 ± 2 nm	Pseudo-spherical morphologies	H ₂ production from ethanol-water	Spectroline model SB-1000P/F lamp (200 W, 365 nm)	The highest rates of H ₂ production were achieved at Au loadings of 0.5, 1 and 2.0 wt% (32, 34 and 33 mmol g ⁻¹ h ⁻¹ , respectively)	138
Au/m-Ta ₂ O ₅	Photodeposition method	AuNP size: 10–20 nm	Mesoporous structure with AuNPs	H ₂ production from methanol; photodegradation of RhB	300 W Xe lamp equipped with an ultraviolet cut-off filter ($\lambda > 400$ nm)	Approximately 98% RhB is degraded in 5 h by 1.0 wt% Au/m-Ta ₂ O ₅	139
Au-P25 TiO ₂	Sol immobilization technique	Au size: 5–10 nm	Spherical Au nanoparticles	Photocatalytic H ₂ evolution	7.2 W Hg vapor light irradiation	H ₂ evolution rate of Au-P25 TiO ₂ is 7.5 times bigger than that of TiO ₂	140
Au/TiO ₂	Photodeposition	Average Au size: 9.4, 7.5, 5.3 and 3.1 nm for Au/TiO ₂ -400, Au/TiO ₂ -500, Au/TiO ₂ -600 and Au/TiO ₂ -700, respectively	Au nanoparticles	H ₂ evolution in photocatalytic reforming of methanol	Xe lamp ($\lambda = 320$ –780 nm) with different optical filters	Synergetic promotion of the photocatalytic activity of TiO ₂ by gold deposition under UV-visible light irradiation	141
Janus and core-shell Au-TiO ₂ , and Au/TiO ₂ nanocomposites	Seeded growth via citrate reduction + encapsulation	Janus Au-TiO ₂ Au size: 30–70 nm	Janus, core-shell and nanocomposites	H ₂ generation from a isopropyl alcohol-aqueous solution	500 W tungsten halogen lamp and a cut-off filter ($\lambda > 400$ nm)	Rate of hydrogen generation using the Janus Au-TiO ₂ was 1.7 times higher than that of their core-shell counterparts, and decreased in the order: Au _{70nm} -TiO ₂ > Au _{50nm} -TiO ₂ > Au _{30nm} -TiO ₂	142
CdS@SiO ₂ //Au@SiO ₂	Encapsulation	Au core size: 19–73 nm	Semiconductor/insulator/metal nanocomposite	H ₂ evolution from 2-propanol-water	Xe lamp ($\lambda > 350$ nm) with light intensity of ca. 100 mW cm ⁻²	Au core of 73 nm gave the optimum enhance factor of 1.5 at $d_{\text{CdS-Au}} = 36$ nm	143
Pt/Au/WO ₃	Photodeposition method and subsequent colloid	Au size in Au/WO ₃ is 13 nm	Nanocomposite	H ₂ evolution from glycerin and 2-propanol, and water oxidation	500 W Xe lamp filtered with a Y-48 filter (450–600 nm: 83 mW cm ⁻²)	AQE of Pt/Au/WO ₃ for water oxidation was calculated to be 0.2% under visible light irradiation from the blue and green LEDs	144
Au/TiO ₂	photodeposition Sol-gel process + deposition	5 nm Au film	Island-like morphology	Photocatalytic reduction of CO ₂ with H ₂ O	UV lamp and green laser	24-fold enhancement in the photocatalytic activity over Au/TiO ₂ in the visible range (532 nm)	145
Au/Pt/TiO ₂	An electrospinning method with postcalcination	Au and Pt nanoparticles with sizes of 5–12 nm	Composite nanofibers	Photocatalytic H ₂ production and CO ₂ conversion	500 W Xe lamp	Au _{0.75} /Pt _{0.25} /TiO ₂ NFs exhibited best photocatalytic activities for both H ₂ generation and CO ₂ reduction	146

main photocatalytic performance and the corresponding references are listed in Table 2 in order to better represent the picture of the area and make comparisons possible.

Abbreviations

AuNPs	Gold nanoparticles
LSPR	Localized surface plasmon resonance
SPR	Surface plasmon resonance
NPs	Nanoparticles
EM	Electromagnetic
AuNRs	Gold nanorods
NIR	Near infrared
AuNSs	Au nanoshells
HRTEM	High resolution transmission electron microscopy
TEM	Transmission electron microscopy
DP	Deposition-precipitation
VB	Valence band
CB	Conduction band
SS	Single-step
MS	Multistep
LED	Light-emitting diode
IPA	2-Propanol
Xenon	Xe
CPH	Colloid photodeposition with a hole scavenger
MOs	Metal oxides
VOCs	Volatile organic compounds
MO	Methyl orange
RhB	Rhodamine B
Meso	Mesocrystal
MB	Methylene blue
1D	One-dimensional
NWs	Nanowires
NTs	Nanotubes
RET	Resonant energy transfer
H ₂	Hydrogen
O ₂	Oxygen
PEC	Photoelectrochemical
3D	Three dimensions
ZFO	ZnFe ₂ O ₄
EPR	Electron paramagnetic resonance
PNP	<i>p</i> -Nitrophenol
4-CP	4-Chlorophenol
NFs	Nanofibers
ESR	Electron spin resonance
SP	Surface plasmon
AuNCs	Au nanocrystals
FDTD	Finite-difference time-domain
TON	Turnover number

Note added in proof

Major contributions to the field of nanogold based plasmonic photocatalysis have appeared since this paper was submitted including theoretical study,¹⁵⁶ applications toward photoreduction,^{157,158}

cross-coupling reactions,¹⁵⁹ acetalisation of aldehydes with methanol,¹⁶⁰ visible-light-driven H₂ evolution from H₂O,^{161–163} ethanol,¹⁶⁴ and water-methanol,¹⁶⁵ PEC water splitting for H₂ generation,¹⁶⁶ and a review.¹⁶⁷

Acknowledgements

Helpful discussions with Dr Wang Dong (Talence) and financial support from the China Scholarship Council (CSC) of the People's Republic of China (grant to C.W.), the Université de Bordeaux and the Centre National de la Recherche Scientifique (CNRS) are gratefully acknowledged.

References

- 1 K. Zeitler, *Angew. Chem., Int. Ed.*, 2009, **48**, 9785–9789.
- 2 X. J. Lang, X. D. Chen and J. C. Zhao, *Chem. Soc. Rev.*, 2014, **43**, 473–486.
- 3 M. C. Daniel and D. Astruc, *Chem. Rev.*, 2004, **104**, 293–346.
- 4 C. Burda, X. B. Chen, R. Narayanan and M. A. El-Sayed, *Chem. Rev.*, 2005, **105**, 1025–1102.
- 5 Y. N. Xia, Y. J. Xiong, B. Lim and S. E. Skrabalak, *Angew. Chem., Int. Ed.*, 2009, **48**, 60–103.
- 6 M. Haruta, *Nature*, 2005, **437**, 1098–1099.
- 7 A. Corma and P. Serna, *Science*, 2006, **313**, 332–334.
- 8 N. Dimitratos, J. A. Lopez-Sanchez and G. J. Hutchings, *Chem. Sci.*, 2012, **3**, 20–44.
- 9 A. S. K. Hashmi and G. J. Hutchings, *Angew. Chem., Int. Ed.*, 2006, **45**, 7896–7936.
- 10 S. Sarina, H. Y. Zhu, Q. Xiao, E. Jaatinen, J. Jia, Y. Huang, Z. Zheng and H. Wu, *Angew. Chem., Int. Ed.*, 2014, **53**, 2935–2940.
- 11 S. Linic, P. Christopher and D. B. Ingram, *Nat. Mater.*, 2011, **10**, 911–921.
- 12 G. H. Chan, J. Zhao, E. M. Hicks, G. C. Schatz and R. P. V. Duyne, *Nano Lett.*, 2007, **7**, 1947–1952.
- 13 A. Marimuthu, J. W. Zhang and S. Linic, *Science*, 2013, **339**, 1590–1593.
- 14 X. N. Guo, C. H. Hao, G. Q. Jin, H. Y. Zhu and X. Y. Guo, *Angew. Chem., Int. Ed.*, 2014, **53**, 1973–1977.
- 15 S. Sarina, E. R. Waclawik and H. Y. Zhu, *Green Chem.*, 2013, **15**, 1814–1833.
- 16 K. Fuku, R. Hayashi, S. Takakura, T. Kamegawa, K. Mori and H. Yamashita, *Angew. Chem., Int. Ed.*, 2013, **52**, 7446–7450.
- 17 K. M. Mayer and J. H. Hafner, *Chem. Rev.*, 2011, **111**, 3828–3857.
- 18 K. Nakayama, K. Tanabe and H. A. Atwater, *Appl. Phys. Lett.*, 2008, **93**, 121904.
- 19 P. K. Jain, I. H. El-Sayed and M. A. El-Sayed, *Nano Today*, 2007, **2**, 18–29.
- 20 C. J. Murphy, A. M. Gole, J. W. Stone, P. N. Sisco, A. M. Alkilany, E. C. Goldsmith and S. C. Baxter, *Acc. Chem. Res.*, 2008, **41**, 1721–1730.

- 21 R. Bardhan, S. Lal, A. Joshi and N. J. Halas, *Acc. Chem. Res.*, 2011, **44**, 936–946.
- 22 R. Mout, D. F. Moyano, S. Rana and V. M. Rotello, *Chem. Soc. Rev.*, 2012, **41**, 2539–2544.
- 23 A. Llevot and D. Astruc, *Chem. Soc. Rev.*, 2012, **41**, 242–257.
- 24 A. Tanaka, K. Hashimoto and H. Kominami, *J. Am. Chem. Soc.*, 2012, **134**, 14526–14533.
- 25 S. S. Rayalu, D. Jose, M. V. Joshi, P. A. Mangrulkar, K. Shrestha and K. Klabunde, *Appl. Catal., B*, 2013, **142**, 684–693.
- 26 S. T. Kochuveedu, Y. H. Jang and D. H. Kim, *Chem. Soc. Rev.*, 2013, **42**, 8467–8493.
- 27 K. M. Mayer and J. H. Hafner, *Chem. Rev.*, 2011, **111**, 3828–3857.
- 28 X. M. Zhang, Y. L. Chen, R. S. Liu and D. P. Tsai, *Rep. Prog. Phys.*, 2013, **76**, 046401.
- 29 K. L. Kelly, E. Coronado, L. L. Zhao and G. C. Schatz, *J. Phys. Chem. B*, 2003, **107**, 668–677.
- 30 M. J. Kale, T. Avanesian and P. Christopher, *ACS Catal.*, 2014, **4**, 116–128.
- 31 L. Brus, *Acc. Chem. Res.*, 2008, **41**, 1742–1749.
- 32 S. Link and M. A. El-Sayed, *Int. Rev. Phys. Chem.*, 2000, **19**, 409–453.
- 33 M. Haruta and M. Daté, *Appl. Catal., A*, 2001, **222**, 427–437.
- 34 M. W. Knight, H. Sobhani, P. Nordlander and N. J. Halas, *Science*, 2011, **332**, 702–704.
- 35 S. Mukherjee, F. Libisch, N. Large, O. Neumann, L. V. Brown, J. Cheng, J. B. Lassiter, E. A. Carter, P. Nordlander and N. J. Halas, *Nano Lett.*, 2013, **13**, 240–247.
- 36 Z. Fang, Z. Liu, Y. Wang, P. M. Ajayan, P. Nordlander and N. J. Halas, *Nano Lett.*, 2012, **12**, 3808–3813.
- 37 Z. Fang, Y. Wang, Z. Liu, A. Schlather, P. M. Ajayan, F. H. L. Koppens, P. Nordlander and N. J. Halas, *ACS Nano*, 2012, **6**, 10222–10228.
- 38 I. Goykhman, B. Desiatov, J. Khurgin, J. Shappir and U. Levy, *Nano Lett.*, 2011, **11**, 2219–2224.
- 39 C. Clavero, *Nat. Photonics*, 2014, **8**, 95–103.
- 40 U. Kreibig and M. Vollmer, *Optical Properties of Metal Clusters*, Springer, Berlin, Germany, 1995.
- 41 E. Dulkeith, T. Niedereichholz, T. A. Klar, J. Feldmann, G. von Plessen, D. I. Gittins, K. S. Mayya and F. Caruso, *Phys. Rev. B: Condens. Matter Mater. Phys.*, 2004, **70**, 205424.
- 42 M. B. Mohamed, V. Volkov, S. Link and M. A. El-Sayed, *Chem. Phys. Lett.*, 2000, **317**, 517–523.
- 43 A. O. Govorov, H. Zhang and Y. K. Gun'ko, *J. Phys. Chem. C*, 2013, **117**, 16616–16631.
- 44 K. Wu, W. E. Rodríguez-Cordoba, Y. Yang and T. Lian, *Nano Lett.*, 2013, **13**, 5255–5263.
- 45 R. A. Molina, D. Weinmann and R. A. Jalabert, *Phys. Rev. B: Condens. Matter Mater. Phys.*, 2002, **65**, 155427.
- 46 G. Baffoua and R. Quidant, *Chem. Soc. Rev.*, 2014, **43**, 3898–3907.
- 47 T. P. White and K. R. Catchpole, *Appl. Phys. Lett.*, 2012, **101**, 073905.
- 48 K. O. Aruda, M. Tagliazucchi, C. M. Sweeney, D. C. Hannah, G. C. Schatz and E. A. Weiss, *Proc. Natl. Acad. Sci. U. S. A.*, 2013, **110**, 4212–4217.
- 49 S. Mukherjee, L. Zhou, A. M. Goodman, N. Large, C. Ayala-Orozco, Y. Zhang, P. Nordlander and N. J. Halas, *J. Am. Chem. Soc.*, 2014, **136**, 64–67.
- 50 H. W. Gao, C. Liu, H. E. Jeong and P. D. Yang, *ACS Nano*, 2012, **6**, 234–240.
- 51 S. Mubeen, G. Hernandez-Sosa, D. Moses, J. Lee and M. Moskovits, *Nano Lett.*, 2011, **11**, 5548–5552.
- 52 Y. Tian and T. Tatsuma, *J. Am. Chem. Soc.*, 2005, **127**, 7632–7637.
- 53 Z. K. Zheng, B. B. Huang, X. Y. Qin, X. Y. Zhang, Y. Dai and M. H. Whangbo, *J. Mater. Chem.*, 2011, **21**, 9079–9087.
- 54 P. Christopher, H. L. Xin and S. Linic, *Nat. Chem.*, 2011, **3**, 467–472.
- 55 J. R. Adleman, D. A. Boyd, D. G. Goodwin and D. Psaltis, *Nano Lett.*, 2009, **9**, 4417–4423.
- 56 X. Chen, H. Y. Zhu, J. C. Zhao, Z. F. Zheng and X. P. Gao, *Angew. Chem., Int. Ed.*, 2008, **47**, 5353–5356.
- 57 D. B. Ingram and S. Linic, *J. Am. Chem. Soc.*, 2011, **133**, 5202–5205.
- 58 M. Grätzel, *Nature*, 2001, **414**, 338–344.
- 59 J. Goldberger, R. He, Y. Zhang, S. Lee, H. Yan, H. J. Choi and P. D. Yang, *Nature*, 2003, **422**, 599–602.
- 60 S. Linc, P. Christopher, H. L. Xin and A. Marimuthu, *Acc. Chem. Res.*, 2013, **46**, 1890–1899.
- 61 J. G. Yu, G. P. Dai and B. B. Huang, *J. Phys. Chem. C*, 2009, **113**, 16394–16401.
- 62 G. C. Schatz, M. A. Young and R. P. Van Duyne, in *Surface-Enhanced Raman Scattering*, ed. K. Kneipp, M. Moskovits and H. Kneipp, Springer, Berlin/Heidelberg, Germany, 2006, vol. 103, pp. 19–45.
- 63 C. Oubre and P. Nordlander, *J. Phys. Chem. B*, 2005, **109**, 10042–10051.
- 64 P. Nordlander, C. Oubre, E. Prodan, K. Li and M. I. Stockman, *Nano Lett.*, 2004, **5**, 899–903.
- 65 S. L. Zou and G. C. Schatz, *Chem. Phys. Lett.*, 2005, **403**, 62–67.
- 66 J. Zhao, A. O. Pinchuk, J. M. McMahon, S. Li, L. K. Ausman, A. L. Atkinson and G. C. Schatz, *Acc. Chem. Res.*, 2008, **41**, 1710–1720.
- 67 M. Rycenga, C. M. Cobley, J. Zeng, W. Y. Li, C. H. Moran, Q. Zhang, D. Qin and Y. N. Xia, *Chem. Rev.*, 2011, **111**, 3669–3712.
- 68 E. Hutter and J. H. Fendler, *Adv. Mater.*, 2004, **16**, 1685–1706.
- 69 P. K. Jain, K. S. Lee, I. H. El-Sayed and M. A. El-Sayed, *J. Phys. Chem. B*, 2006, **110**, 7238–7248.
- 70 K. Yamada, K. Miyajima and F. Mafun, *J. Phys. Chem. C*, 2007, **111**, 11246–11251.
- 71 S. Link and M. A. El-Sayed, *J. Phys. Chem. B*, 1999, **103**, 4212–4217.
- 72 C. M. Cobley, M. Rycenga, F. Zhou, Z. Y. Li and Y. Xia, *J. Phys. Chem. C*, 2009, **113**, 16975–16982.
- 73 N. Li, P. X. Zhao and D. Astruc, *Angew. Chem., Int. Ed.*, 2014, **53**, 1756–1789.
- 74 X. Huang, I. H. El-Sayed, W. Qian and M. A. El-Sayed, *J. Am. Chem. Soc.*, 2006, **128**, 2115–2120.

- 75 H. Chen, L. Shao, Q. Li and J. Wang, *Chem. Soc. Rev.*, 2013, **42**, 2679–2724.
- 76 P. K. Jain and M. A. El-Sayed, *Nano Lett.*, 2007, **7**, 2854–2858.
- 77 A. Bansal and S. S. Verma, *Plasmonics*, 2014, **9**, 335–341.
- 78 K. W. Choi, D. Y. Kim, X. L. Zhong, Z. Y. Li, S. H. Im and O. O. Park, *CrystEngComm*, 2013, **15**, 252–258.
- 79 S. Eustis and M. A. El-Sayed, *Chem. Soc. Rev.*, 2006, **35**, 209–217.
- 80 J. J. Mock, M. Barbic, D. R. Smith, D. A. Schultz and S. Schultz, *J. Chem. Phys.*, 2002, **116**, 6755–6759.
- 81 Y. Sun and Y. Xia, *Anal. Chem.*, 2002, **74**, 5297–5305.
- 82 S. K. Ghosh, S. Nath, S. Kundu, K. Esumi and T. Pal, *J. Phys. Chem. B*, 2004, **108**, 13963–13971.
- 83 S. Sarina, H. Zhu, E. Jaatinen, Q. Xiao, H. Liu, J. Jia and J. Zhao, *J. Am. Chem. Soc.*, 2013, **135**, 5793–5801.
- 84 S. Sarina, S. Bai, Y. Huang, C. Chen, J. Jia, E. Jaatinen and H. Zhu, *Green Chem.*, 2014, **16**, 331–341.
- 85 K. Awazu, M. Fujimaki, C. Rockstuhl, J. Tominaga, H. Murakami, Y. Ohki and T. Watanabe, *J. Am. Chem. Soc.*, 2008, **130**, 1676–1680.
- 86 D. Tsukamoto, Y. Shiraishi, Y. Sugano, S. Ichikawa, S. Tanaka and T. Hirai, *J. Am. Chem. Soc.*, 2012, **134**, 6309–6315.
- 87 C. G. Silva, R. Juárez, T. Marino, R. Molinari and H. García, *J. Am. Chem. Soc.*, 2011, **133**, 595–602.
- 88 A. Tanaka, K. Fuku, T. Nishi, K. Hashimoto and H. Kominami, *J. Phys. Chem. C*, 2013, **117**, 16983–16989.
- 89 A. Tanaka, S. Sakaguchi, K. Hashimoto and H. Kominami, *Catal. Sci. Technol.*, 2014, **4**, 1931–1938.
- 90 Q. Zhang, D. Q. Lima, I. Lee, F. Zaera, M. F. Chi and Y. D. Yin, *Angew. Chem., Int. Ed.*, 2011, **50**, 7088–7092.
- 91 S. K. Cushing, J. T. Li, F. Meng, T. R. Senty, S. Suri, M. J. Zhi, M. Li, A. D. Bristow and N. Q. Wu, *J. Am. Chem. Soc.*, 2012, **134**, 15033–15041.
- 92 C. D. Pina, E. Falletta and M. Rossi, *Chem. Soc. Rev.*, 2012, **41**, 350–369.
- 93 G. L. Hallett-Tapley, M. J. Silvero, M. González-Béjar, M. Grenier, J. C. Netto-Ferreira and J. C. Scaiano, *J. Phys. Chem. C*, 2011, **115**, 10784–10790.
- 94 G. L. Hallett-Tapley, M. J. Silvero, C. J. Bueno-Alejo, M. González-Béjar, C. D. McTiernan, M. Grenier, J. C. Netto-Ferreira and J. C. Scaiano, *J. Phys. Chem. C*, 2013, **117**, 12279–12288.
- 95 X. Q. Huang, Y. J. Li, Y. Chen, H. L. Zhou, X. F. Duan and Y. Huang, *Angew. Chem., Int. Ed.*, 2013, **52**, 6063–6067.
- 96 A. Tanaka, K. Hashimoto and H. Kominami, *Chem. Commun.*, 2011, **47**, 10446–10448.
- 97 Y. Sugano, Y. Shiraishi, D. Tsukamoto, S. Ichikawa, S. Tanaka and T. Hirai, *Angew. Chem., Int. Ed.*, 2013, **52**, 5295–5299.
- 98 X. G. Zhang, X. B. Ke and H. Y. Zhu, *Chem. – Eur. J.*, 2012, **18**, 8048–8056.
- 99 A. Pineda, L. Gomez, A. M. Balu, V. Sebastian, M. Ojeda, M. Arruebo, A. A. Romero, J. Santamaria and R. Luque, *Green Chem.*, 2013, **15**, 2043–2049.
- 100 L. Q. Liu, S. X. Ouyang and J. H. Ye, *Angew. Chem., Int. Ed.*, 2013, **52**, 6689–6693.
- 101 A. Tanaka, Y. Nishino, S. Sakaguchi, T. Yoshikawa, K. Imamura, K. Hashimoto and H. Kominami, *Chem. Commun.*, 2013, **49**, 2551–2553.
- 102 A. Tanaka, S. Sakaguchi, K. Hashimoto and H. Kominami, *ACS Catal.*, 2013, **3**, 79–85.
- 103 Y. Horiguchi, T. Kanda, K. Torigoe, H. Sakai and M. Abe, *Langmuir*, 2014, **30**, 922–928.
- 104 R. Sellappan, M. G. Nielsen, F. González-Posada, P. C. K. Vesborg, I. Chorkendorff and D. Chakarov, *J. Catal.*, 2013, **307**, 214–221.
- 105 H. Zhu, X. Ke, X. Yang, S. Sarina and H. Liu, *Angew. Chem., Int. Ed.*, 2010, **49**, 9657–9661.
- 106 X. Ke, S. Sarina, J. Zhao, X. Zhang, J. Chang and H. Zhu, *Chem. Commun.*, 2012, **48**, 3509–3511.
- 107 X. B. Ke, X. G. Zhang, J. Zhao, S. Sarina, J. Barry and H. Y. Zhu, *Green Chem.*, 2013, **15**, 236–244.
- 108 S. Naya, K. Kimura and H. Tada, *ACS Catal.*, 2013, **3**, 10–13.
- 109 J. Zhao, Z. F. Zheng, S. Bottle, A. Chou, S. Sarina and H. Y. Zhu, *Chem. Commun.*, 2013, **49**, 2676–2678.
- 110 M. González-Béjar, K. Peters, G. L. Hallett-Tapley, M. Grenier and J. C. Scaiano, *Chem. Commun.*, 2013, **49**, 1732–1734.
- 111 Y. Ide, N. Nakamura, H. Hattori, R. Ogino, M. Ogawa, M. Sadakane and T. Sano, *Chem. Commun.*, 2011, **47**, 11531–11533.
- 112 W. B. Hou, Z. W. Liu, P. Pavaskar, W. H. Hung and S. B. Cronin, *J. Catal.*, 2011, **277**, 149–153.
- 113 F. Pincella, K. Isozaki and K. i. Miki, *Light: Sci. Appl.*, 2014, **3**, e133.
- 114 J. W. Lu, P. Zhang, A. Li, F. L. Su, T. Wang, Y. Liu and J. L. Gong, *Chem. Commun.*, 2013, **49**, 5817–5819.
- 115 S. Y. Zhu, S. J. Liang, Q. Gu, L. Y. Xie, J. X. Wang, Z. X. Ding and P. Liu, *Appl. Catal., B*, 2012, **119**, 146–155.
- 116 Y. L. Liu, W. Shu, Z. Y. Peng, K. Q. Chen and W. Chen, *Catal. Today*, 2013, **208**, 28–34.
- 117 G. K. Naik, P. M. Mishra and K. Parida, *Chem. Eng. J.*, 2013, **229**, 492–497.
- 118 Z. Bian, T. Tachikawa, P. Zhang, M. Fujitsuka and T. Majima, *J. Am. Chem. Soc.*, 2014, **136**, 458–465.
- 119 S. T. Kochuveedu, D. Kim and D. H. Kim, *J. Phys. Chem. C*, 2012, **116**, 2500–2506.
- 120 J. J. Chen, J. C. S. Wu, P. C. Wu and D. P. Tsai, *J. Phys. Chem. C*, 2012, **116**, 26535–26542.
- 121 J. Y. Lan, X. M. Zhou, G. Liu, J. G. Yu, J. C. Zhang, L. J. Zhi and G. J. Nie, *Nanoscale*, 2011, **3**, 5161–5167.
- 122 Y. Wen, B. T. Liu, W. Zeng and Y. H. Wang, *Nanoscale*, 2013, **5**, 9739–9746.
- 123 M. Misra, P. Kapur and M. L. Singla, *Appl. Catal., B*, 2014, **150**, 605–611.
- 124 S. Naya, T. Nikawa, K. Kimura and H. Tada, *ACS Catal.*, 2013, **3**, 903–907.
- 125 A. Tanaka, A. Ogino, M. Iwaki, K. Hashimoto, A. Ohnuma, F. Amano, B. Ohtani and H. Kominami, *Langmuir*, 2012, **28**, 13105–13111.
- 126 L. Gomez, V. Sebastian, M. Arruebo, J. Santamaria and S. B. Cronin, *Phys. Chem. Chem. Phys.*, 2014, **16**, 15111–15116.

- 127 F. Wang, C. H. Li, H. J. Chen, R. N. Jiang, L. D. Sun, Q. Li, J. F. Wang, J. C. Yu and C. H. Yan, *J. Am. Chem. Soc.*, 2013, **135**, 5588–5601.
- 128 Z. Liu, W. Hou, P. Pavaskar, M. Aykol and S. B. Cronin, *Nano Lett.*, 2011, **11**, 1111–1116.
- 129 S. C. Warren and E. Thimsen, *Energy Environ. Sci.*, 2012, **5**, 5133–5146.
- 130 J. Chen, J. C. S. Wu, P. C. Wu and D. P. Tsai, *J. Phys. Chem. C*, 2011, **115**, 210–216.
- 131 S. Mubeen, J. Lee, N. Singh, S. Krämer, G. D. Stucky and M. Moskovits, *Nat. Nanotechnol.*, 2013, **8**, 247–251.
- 132 Y. C. Pu, G. M. Wang, K. D. Chang, Y. C. Ling, Y. K. Lin, B. C. Fitzmorris, C. M. Liu, X. H. Lu, Y. X. Tong, J. Z. Zhang, Y. J. Hsu and Y. Li, *Nano Lett.*, 2013, **13**, 3817–3823.
- 133 A. Tanaka, K. Nakanishi, R. Hamada, K. Hashimoto and H. Kominami, *ACS Catal.*, 2013, **3**, 1886–1891.
- 134 J. Fang, S. W. Cao, Z. Wang, M. M. Shahjamali, S. C. J. Loo, J. Barber and C. Xue, *Int. J. Hydrogen Energy*, 2012, **37**, 17853–17861.
- 135 P. A. DeSario, J. J. Pietron, D. E. DeVantier, T. H. Brintlinger, R. M. Stroud and D. R. Rolison, *Nanoscale*, 2013, **5**, 8073–8083.
- 136 A. Sheikh, A. Yengantiwar, M. Deo, S. Kelkar and S. Ogale, *Small*, 2013, **9**, 2091–2096.
- 137 A. Tanaka, S. Sakaguchi, K. Hashimoto and H. Kominami, *Catal. Sci. Technol.*, 2012, **2**, 907–909.
- 138 V. Jovic, W. T. Chen, D. Sun-Waterhouse, M. G. Blackford, H. Idriss and G. I. N. Waterhouse, *J. Catal.*, 2013, **305**, 307–317.
- 139 C. Zhou, L. Shang, H. Yu, T. Bian, L. Z. Wu, C. H. Tung and T. Zhang, *Catal. Today*, 2014, **225**, 158–163.
- 140 J. B. Priebe, M. Karnahl, H. Junge, M. Beller, D. Hollmann and A. Brückner, *Angew. Chem., Int. Ed.*, 2013, **52**, 11420–11424.
- 141 J. Q. Yan, G. J. Wu, N. J. Guan and L. D. Li, *Chem. Commun.*, 2013, **49**, 11767–11769.
- 142 Z. W. Seh, S. H. Liu, M. Low, S. Y. Zhang, Z. H. Liu, A. Mlayah and M. Y. Han, *Adv. Mater.*, 2012, **24**, 2310–2314.
- 143 T. Torimoto, H. Horibe, T. Kameyama, K. Okazaki, S. Ikeda, M. Matsumura, A. Ishikawa and H. Ishihara, *J. Phys. Chem. Lett.*, 2011, **2**, 2057–2062.
- 144 A. Tanaka, K. Hashimoto and H. Kominami, *J. Am. Chem. Soc.*, 2014, **136**, 586–589.
- 145 W. B. Hou, W. H. Hung, P. Pavaskar, A. Goepfert, M. Aykol and S. B. Cronin, *ACS Catal.*, 2011, **1**, 929–936.
- 146 Z. Y. Zhang, Z. Wang, S. W. Cao and C. Xue, *J. Phys. Chem. C*, 2013, **117**, 25939–25947.
- 147 W. Hou and S. B. Cronin, *Adv. Funct. Mater.*, 2013, **23**, 1612–1619.
- 148 Z. H. Zhang, L. B. Zhang, M. N. Hedhili, H. N. Zhang and P. Wang, *Nano Lett.*, 2013, **13**, 14–20.
- 149 F. Le, D. W. Brandl, Y. A. Urzhumov, H. Wang, J. Kundu, N. J. Halas, J. Aizpurua and P. Nordlander, *ACS Nano*, 2008, **2**, 707–718.
- 150 C. Oubre and P. Nordlander, *J. Phys. Chem. B*, 2004, **108**, 17740–17747.
- 151 H. Wang, T. You, W. Shi, J. Li and L. Guo, *J. Phys. Chem. C*, 2012, **116**, 6490–6494.
- 152 N. Zhou, L. Polavarapu, N. Y. Gao, Y. L. Pan, P. Y. Yuan, Q. Wang and Q. H. Xu, *Nanoscale*, 2013, **5**, 4236–4241.
- 153 J. Zhu, J. J. Li and J. W. Zhao, *Plasmonics*, 2014, **9**, 435–441.
- 154 D. B. Ingram, P. Christopher, J. L. Bauer and S. Linic, *ACS Catal.*, 2011, **1**, 1441–1447.
- 155 P. Christopher, D. B. Ingram and S. Linic, *J. Phys. Chem. C*, 2010, **114**, 9173–9177.
- 156 A. Manjavacas, J. G. Liu, V. Kulkarni and Peter Nordlander, *ACS Nano*, 2014, DOI: 10.1021/nn502445f.
- 157 S.-i. Naya, T. Niwa, T. Kume and H. Tada, *Angew. Chem., Int. Ed.*, 2014, **53**, 7305–7309.
- 158 H. Lin, L. Ding, Z. Pei, Y. Zhou, J. Long, W. Deng and X. Wang, *Appl. Catal., B*, 2014, **160**, 98–105.
- 159 Q. Xiao, S. Sarina, A. Bo, J. Jia, H. Liu, D. P. Arnold, Y. Huang, H. Wu and H. Zhu, *ACS Catal.*, 2014, **4**, 1725–1734.
- 160 X. Zhang, A. Du, H. Zhu, J. Jia, J. Wang and X. Ke, *Chem. Commun.*, DOI: 10.1039/c4cc03225j.
- 161 J. S. DuChene, B. C. Sweeny, A. C. Johnston-Peck, D. Su, E. A. Stach and W. D. Wei, *Angew. Chem., Int. Ed.*, 2014, **53**, 1–6.
- 162 S. Pany, B. Naik, S. Martha and K. Parida, *ACS Appl. Mater. Interfaces*, 2014, **6**, 839–846.
- 163 Z. Zhang, A. Li, S.-W. Cao, M. Bosman, S. Li and C. Xue, *Nanoscale*, 2014, **6**, 5217–5222.
- 164 S. S. Rayalu, D. Jose, P. A. Mangrulkar, M. Joshi, G. Hippargi, K. Shrestha and K. Klabunde, *Int. J. Hydrogen Energy*, 2014, **39**, 3617–3624.
- 165 Z. Zheng, T. Tachikawa and T. Majima, *J. Am. Chem. Soc.*, 2014, **136**, 6870–6873.
- 166 J. Li, S. K. Cushing, P. Zheng, T. Senty, F. Meng, A. D. Bristow, A. Manivannan and N. Wu, *J. Am. Chem. Soc.*, 2014, **136**, 8438–8449.
- 167 R. B. Jiang, B. X. Li, C. H. Fang and J. F. Wang, *Adv. Mater.*, 2014, DOI: 10.1002/adma.201400203.